Estimating the optical depth of Saturn's main rings using the Cassini Langmuir Probe

Georgios Xystouris [ORCID],[1]* Christopher S. Arridge,[1]* Michiko M. Morooka[2] and Jan-Erik Wahlund[2]

[1]*Department of Physics, Lancaster University, Bailrigg, Lancaster LA1 4YB, UK*
[2]*Swedish Institute of Space Physics, Box 537, SE-751 21, Uppsala, Sweden*

ABSTRACT

A Langmuir Probe (LP) measures currents from incident charged particles as a function of the applied bias voltage. While onboard a spacecraft the particles are either originated from the surrounding plasma, or emitted (e.g. through photoemission) from the spacecraft itself. The obtained current–voltage curve reflects the properties of the plasma in which the probe is immersed into, but also any photoemission due to illumination of the probe surface: As photoemission releases photoelectrons into space surrounding the probe, these can be recollected and measured as an additional plasma population. This complicates the estimation of the properties of the ambient plasma around the spacecraft. The photoemission current is sensitive to the extreme ultraviolet (UV) part of the spectrum, and it varies with the illumination from the Sun and the properties of the LP surface material, and any variation in the photoelectrons irradiance can be measured as a change in the current voltage curve. Cassini was eclipsed multiple times by Saturn and the main rings over its 14 yr mission. During each eclipse the LP recorded dramatic changes in the current–voltage curve, which were especially variable when Cassini was in shadow behind the main rings. We interpret these variations as the effect of spatial variations in the optical depth of the rings and hence use the observations to estimate the optical depth of Saturn's main rings. Our estimates are comparable with UV optical depth measurements from Cassini's remote sensing instruments.

Key words: opacity – plasmas – instrumentation: miscellaneous – eclipses – planets and satellites: rings.

1. INTRODUCTION

A multitude of studies have established that Enceladus is the main plasma source of Saturn's inner magnetosphere (e.g. Pontius & Hill 2006), but additional minor sources were found, such as Rhea (e.g. Tseng et al. 2011), the main rings (e.g. Johnson et al. 2006), and the ionosphere (e.g. Hadid et al. 2019). These plasma sources have been probed in detail by the comprehensive suite of instruments carried by Cassini, including the Langmuir Probe (LP; e.g. Gustafsson & Wahlund 2010), the Radio and Plasma Wave Science (RPWS) instrument (e.g. Persoon et al. 2006), and the Cassini Plasma Spectrometer (CAPS; e.g. Coates et al. 2005). Typically, these observations, particularly those made by CAPS and LP, are contaminated by photoelectrons generated through the interaction of the sunlight with the spacecraft, emitting electrons from the surface and creating an electron 'cloud' around the spacecraft.

The LP can estimate both the electron and ion density by analysing the current–voltage (I–V) curve generated by the corresponding particles as they interact with the probe. Unfortunately, since the LP only measures the current as a function of bias voltage, it cannot separate electrons and ions from these different magnetospheric and spacecraft sources—particularly spacecraft photoelectrons from magnetospheric electrons. One way we might be able to do this

is to study the changes in measured I–V curves as the spacecraft transitions into shadow and, therefore, where the photoelectron population should disappear. Accordingly, in this study we set out to study the impact of sunlight on the LP measurements, and examine how the probe's behaviour changes when transitioning into and out of sunlight. We use all available solar eclipses as seen from Cassini by either Saturn or its rings, i.e. periods where Cassini goes into the shadow of Saturn or its rings. It was realized that these measurements also provide an estimate of the opacity of the rings.

The intensity of light through an opaque medium falls exponentially with distance, and that 'e-folding' factor is known as the optical depth, τ, and is related to the product of the opacity and thickness of the medium. An optical depth of 1 means that the intensity of the light has dropped by a factor of 1/e, or about 63 per cent. Saturn's rings can be divided into two categories: the dense rings, which include A, B, and C rings, and the tenuous rings, which include the D, E, and G rings. One of the first studies on ring opacity was from Esposito et al. (1983), where, using stellar occultations from the ultraviolet (UV) spectrometer onboard Voyager 2 during its flyby of Saturn they calculated the optical depth of the rings in the ultraviolet C (UV-C) range ($100-280$ nm): The D ring appeared tenuous, with $\tau \approx 0$; the C ring had a quite low normal optical depth with $\tau \sim 0.1$; the B ring was the most opaque one, with τ from 0.6 to well over 2.6; the Cassini Division had a C-like opacity, and the A ring was opaque with $\tau \sim 0.5$.

Later studies used data from the Cassini era, so a larger amount of data was available over a wider time-base and in different

* E-mail: g.xystouris@lancaster.ac.uk (GX); c.arridge@lancaster.ac.uk (CSA)

seasonal geometries. Colwell et al. (2009, 2010), using data from Cassini's ultraviolet imaging spectrograph (UVIS) operating in the 110−190 nm spectral range, showed that the optical depth for the A ring was between 0.5 and 1 without large variations, but the B ring was well above 1 and varying significantly over distance, sometimes reaching values up to 5. The optical depths for the C ring and Cassini Division were similar and closer to 0, at around 0.1 – i.e. the light intensity dropped by about 9.5 per cent. This 'division' between the A–B rings and C–D rings was reported in other wavelengths too, e.g. by Hedman et al. (2013) where, using data from Cassini's Visual and Infrared Mapping Spectrometer (VIMS; operating in two different spectral ranges 350−1050 nm and 850−5200 nm) they reported a uniform distribution of a visible and near-UV absorbers across the A ring, the Cassini Division, and the outer B ring, that increases towards the inner B ring and stays high over the C ring—hence a higher reflectivity of the A and B rings.

Farrell et al. (2017), using RPWS data from Saturn Orbit Insertion, reported an inverse correlation between electron density and ring opacity from the A ring to C ring, including the Cassini Division, with the density of the B ring found to be the highest, as it is the most optically thick. A series of studies using the LP studied the properties of Saturn's ionosphere in and out of shadow to examine the effects of attenuated light on photochemical processes and observed changes connected to the opacity of the rings. Wahlund et al. (2018) used LP data during the Grand Finale orbits—where the spacecraft conducted a series of orbits passing in-between Saturn the D ring (Ida 2019)—and, based on the photoionization of Saturn's ionosphere, reported that the A and most of the B ring are opaque to solar extreme ultraviolet (EUV), as there was very little plasma within the regions of the rings' shadows. The Cassini Division was found to be less opaque to EUV, and the C and D rings are transparent to EUV, as no plasma changes were reported in their shadows. Hadid et al. (2018), using the same instrument and for the same period, also reported that while the A ring shows a somewhat uniform opacity in EUV throughout the entire extent of the ring, the B ring has a non-uniform EUV opacity that is probably connected with the reported altitude-latitude variation of the proximal orbits (e.g. Wahlund et al. 2018; Persoon et al. 2019).

In this paper, we identify all the eclipses of Cassini by Saturn and the main rings. We study the behaviour of the measured I–V curves through these eclipses and used the measured variations to infer photoemission rate which we use as a proxy for the optical depth between the spacecraft and the Sun. Hence, we estimate the optical depth of Saturn's main rings using the LP.

2. PROBE DESIGN AND OPERATION/METHODS

The principle of a LP operation is the measurement of the I–V curve, which is a characteristic of both the probe and the plasma environment, and the properties of the plasma (density, temperature, ion mass, etc.) can be estimated based on the measured I–V curve (e.g. Mott-Smith & Langmuir 1926; Hoegy & Brace 1999). When a bias voltage is applied to the probe, a sheath is created around the LP repelling the low-energy same-charge particles and attracting the oppositely-charged ones—the bias voltage can be either positive or negative. As an example, if we assume that the LP is positively charged it will attract all the electrons—both the ambient plasma electrons and photoelectrons—while it will repel almost all the ions—some high-energy ions will overcome the potential and will interact with the instrument generating a current. The inverse picture takes place when the LP is negatively charged. The generated current

is a function of the plasma properties (density, temperature, ion mass, etc.), but also it is a function of the potential structure around the probe and the probe geometry.

Fig. 1 shows an example of the possible interactions of the ambient plasma and sunlight with a probe. As the probe is a metallic sphere additional non-ambient-plasma electron sources appear: the secondary electrons (electrons generated after an energetic electron/ion impact with the probe) and the photoelectrons (electron emitted due to the incident sunlight interacting with the probe or the spacecraft). Those electrons will still be measured as ambient plasma electrons, as the LP cannot distinguish between them.

Cassini's LP is a 5 cm diameter titanium spherical probe, baked at a high temperature in a nitrogen atmosphere to produce a titanium nitride coating (Whalström et al. 1992). It is located at the end of a boom, extending the probe 1.5 m away from the spacecraft body in order to receive as little contamination by photoelectrons coming from the spacecraft as possible (Gurnett et al. 2004). Also, to minimize disturbances from the boom and Cassini itself, the last 10.9 cm of the boom is very thin (6.35 mm diameter rod) and is kept under the same potential as the probe (Jacobsen et al. 2009).

For each sweep, a bias voltage from −32 to +32 V is applied over 256 points, each done twice to allow the bias potential to settle and currents to readjust, producing 512 points. This is done rapidly over the course of 0.5 s and carried out periodically to provide a sampling of the plasma at different locations. The typical period is around 10 min, but it can vary for some special orbits, e.g. for targeted moon flybys the sweep frequency drops down to 10 s and the bias voltage ranges from −5 to +5 V. The currents are usually largest under positive bias.

Since the LP is away from the spacecraft's body, its potential is simply the potential of the spacecraft's electrostatic field at that distance; this is the instrument's floating potential U_{fl}. As Cassini moves through plasma, and as electrons are lighter, hence moving faster than the ions, more electrons will hit the spacecraft, charging it negatively; this charge can give the spacecraft potential, $U_{\text{s/c}}$, which is the potential relative to the plasma; comparing the two potentials: $|U_{\text{s/c}}| < |U_{\text{fl}}|$. In the inner magnetosphere, the spacecraft potential is typically negative; however, at very low and very high altitudes in sunlight the photoemission may dominate over the electron plasma current, setting a positive potential to the spacecraft (Fahleson 1967). The total potential of the LP (relative to the plasma potential) is the sum of the floating potential, plus the applied bias voltage, U_{b}: $U_{\text{total}} = U_{\text{b}} + U_{\text{fl}}$. When the bias voltage applied is equal to the $−U_{\text{fl}}$, the total voltage the LP is under is equal to 0; this is the 'changing' point for the attracted particles. Hence, the LP is negatively charged in the interval −32 V to $−U_{\text{fl}}$, attracting ions (the 'ion current' region), and positively charged in the interval $−U_{\text{fl}}$ to +32 V, attracting electrons (the 'electron current' region). The current for the negatively charged region can be symbolized as I_{-} and for the positive as I_{+}. We must also note that when Cassini is in sunlight there is always a photoelectron current from the LP, regardless of the probe charge—the probe charge changes though whether the photoelectrons will return to the probe or not.

In dense ($\sim 10^7$ m^{-3}) plasma regions, the I–V curve can be fitted with model currents giving estimates of the surrounding plasma properties (e.g. Gustafsson & Wahlund 2010; Holmberg et al. 2012). This method is reliable only if the Debye length of the surrounding plasma is large compared with the probe radius (Laframboise 1966); this applies to our study, as there were only six data points of the entire data base with a Debye length smaller than the LP radius. To estimate the parameters of ions in the plasma, we can use a linear
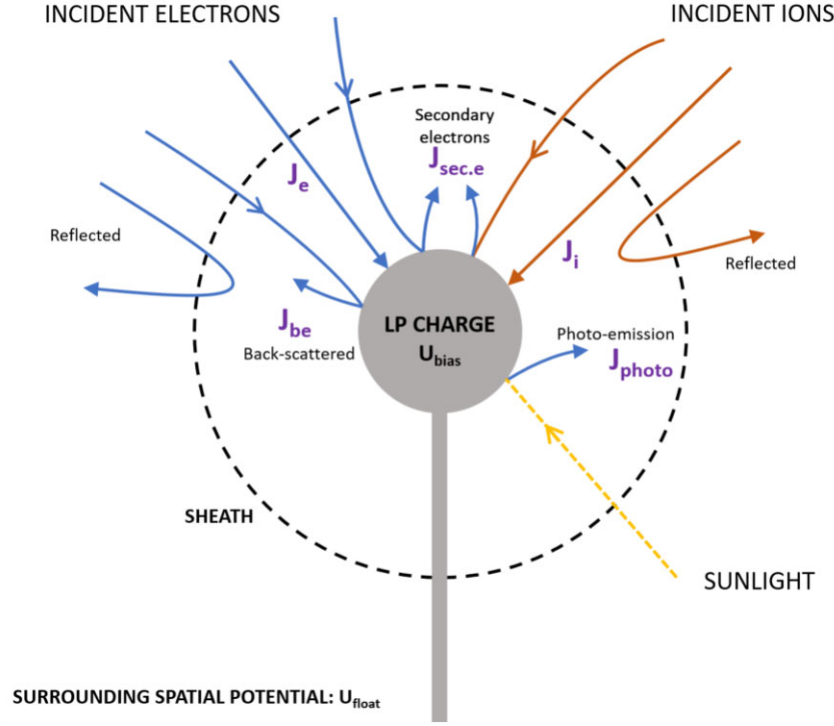
Figure 1. Schematic of all the possible interactions of the plasma particles and sunlight with the LP. The left-hand-side arrows (in blue) correspond to the incident electrons, the right-hand-side arrows (in brown) to the incident ions, and in the lower right corner (dashed yellow) is the sunlight. The generated current from each interaction is in purple.

approximation based on the work of Fahleson ([1967](#)). The ion current can be expressed as

$$I_i = I_{i,0} \left(1 - \frac{q_i (U_{fl} + U_b)}{\frac{m_i u_i^2}{2} + k_B T_i} \right) \tag{1}$$

where

$$I_{i,0} \approx -A_{LP} n_i q_i \left(\frac{u_i^2}{16} + \frac{k_B T_i}{2\pi m_i} \right)^{1/2} \tag{2}$$

where q_i is the ion charge, m_i the ion mass, T_i the ion temperature, u_i the bulk ion speed, A_{LP} is the surface area of the LP, and k_B is the Boltzmann constant, U_b is the applied bias voltage, and U_{fl} is the floating potential of the probe. Taking the above equations, adding the photoelectron current, I_{ph} and replacing with

$$m = I_{i,0} \left(1 - \frac{q_i U_{fl}}{\frac{m_i u_i^2}{2} + k_B T_i} \right) + I_{ph} \tag{3}$$

and

$$b = -\frac{I_{i,0} q_i}{\frac{m_i u_i^2}{2} + k_B T_i} \tag{4}$$

we get the linear equation: $I_- = b U_{bias} + m$, that can be applied to the region of the ion current. As the region from about -5 V to $-U_{fl}$ is not linear – due to additional current sources, such as secondary electrons and energetic electrons that can overcome the negative potential and interact with the probe – we apply the equations above to the region from -32 to -5 V. We also need to note that when the LP is negatively charged, the measured current is the sum of the ion current, the photoelectron current, and the secondary electron

current: $I_- = I_i + I_{ph} + I_{sec.e}$. A simple way to see this is to think that a positive charge captured by the LP can be described equally as a negative charge leaving the surface. We will discuss further the impact of the secondary electrons later in this chapter.

To estimate the electron parameters, we are using a multiple-population model as described on Gustafsson & Wahlund ([2010](#)). The electron density distribution for energies up to 10 eV, which is the LP energy threshold can be described by a superposition of multiple electron populations, each one following a Maxwellian distribution, and there can be up to three populations depending on the best fit on the I–V curve. The shape of the I–V curve depends on the number of populations, the electron density, and the electron temperature. Earlier works often assumed that the first population corresponded to photoemission, but this is not always correct—one of the major points is that this assumption can collapse is when the best fit gives us a one-population model.

Fig. [2](#) shows an example of an I–V curve during an LP sweep. For this sweep a three-population model was used, as it had the best fit compared with a one- or two-population model.

It should be noted that even though we are using the above model, the multiple electron populations may represent a non-Maxwellian structure in the ambient electron population surrounding the spacecraft. So far, we have not found any evidence supporting this theory, but the problem we are facing is that the LP measurements can be approximated equally well using a Maxwellian, or a kappa distribution, and the Maxwellian only fails in regions where the measurements are of poor quality, i.e. regions with poor data coverage/data gaps.

Lastly, we need to mention that an ongoing and open area of study is secondary electron current from the LP. Secondary electrons are the result of primary energetic electrons moving through a
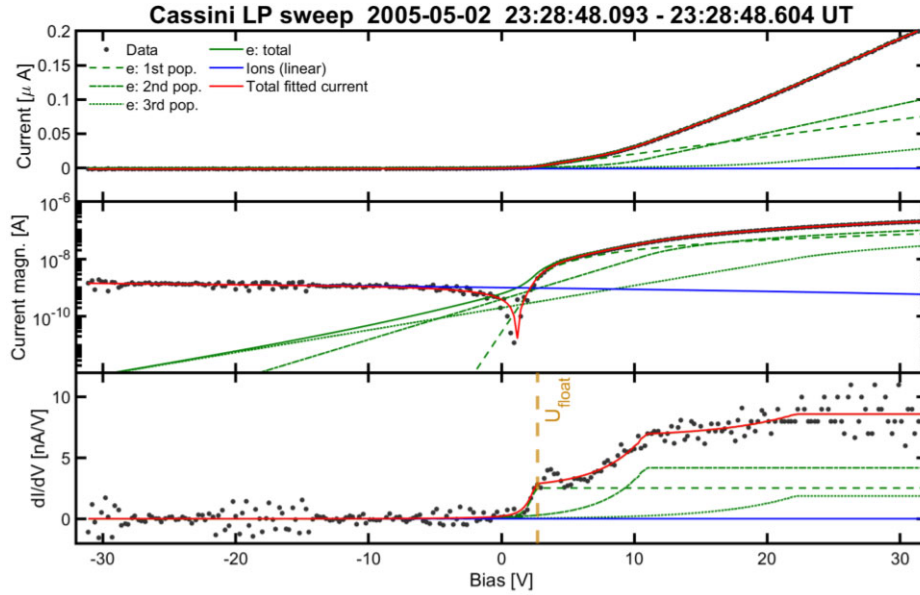
Figure 2. I–V curve of a sweep. The first and second panel show the current in linear and logarithmic scale, and the third panel shows the current gradient with respect to the bias voltage. The green lines show the electron theoretical currents (dashed: first population, dash–dotted: second population, dotted: third population, and solid: total electron current), the blue line shows the ion current, and the red one is the total theoretical current. Each 'knee' on the gradient denotes the existence of a different electron population. Also, the first 'knee' on the gradient shows the floating potential, $-U_{fl}$, of the instrument. Plot similar to Fig. 1 from Gustafsson & Wahlund (2010).

material and transferring energy to electrons in the material that can then escape if they have sufficient energy (e.g. Whipple 1981). Garnier et al. (2013) reported an influence of secondary electrons in the LP measurements around $L \sim 6{-}10$ due to high-energy electrons ($250{-}450$ eV) in that region, while Thomsen et al. (2016) reported the existence of high-energy electrons (in energies 5797, 2054, and 728 eV) in the inner magnetosphere: The inner boundary for penetration of the high-energy electrons was between $L \sim 4.7$ and 8.4, with a median near $L = 6.2$. We estimate that the secondary electrons will not affect our results though—at least not dramatically—as only a handful of eclipses by Saturn were close to $\sim 8R_S$, while the rest were within $6R_S$.

2.1 Photoemission

Photoemission is the emission of the electrons from a surface due to sunlight in the EUV region of the spectrum (between 10 and 120 nm; e.g. Whipple 1981 and references therein). All metals are subject to photoemission in space. If the LP is negatively charged, the photoelectrons will be repelled, creating a current away from the probe, while if the probe is positively charged, it will attract a fraction of those electrons back to the probe as a photoelectron current. The photoemission current varies, depending on: the surface material and how the surface was processed (quenching, tempering, heat treating, etc.), the intensity and spectral distribution of sunlight, and the angle and polarization of the incident sunlight (e.g. Grard 1973; Diaz-Aguado et al. 2018). By way of example, for the LP on Pioneer Venus Orbiter variations in photoemission due to variations in sunlight were used by Brace et al. (1988) to estimate solar irradiance in the EUV over time. The energy distribution of the emitted photoelectrons can be approximated by a Maxwellian distribution (Grard 1973). Typically, as we will show later in the work, the LP photocurrent is in the range of $10^{-10}{-}10^{-8}$ A cm^{-2}, range which the instrument is capable of measuring, with an energy of $1{-}2$ eV.

For a LP that is small compared with the Debye length, Grard (1973) described the photoemission currents:

$$I = \begin{cases} I_0 & \\ I_0 \left(1 - \frac{e\varphi}{kT}\right) \exp\left[e\varphi/kT\right] \end{cases} \quad for \quad \begin{matrix} \varphi \geq 0 \\ \varphi < 0 \end{matrix} \quad (5)$$

where I_0 is a constant that is determined by the measurements, and φ is defined as

$$\varphi = U_{\text{plasma}} - U_{\text{bias}}. \quad (6)$$

However, the constant I_0 cannot be calculated that easily on Cassini's LP due to additional parameters affecting the generation of photoelectrons; one of them is the rod connecting the LP with the spacecraft. In any given moment that the LP is not in a body's or the spacecraft's shadow, while the sunlight illuminates half of the probe, the photoelectron current generated from the rod varies, as it depends on the part of the rod that's shadowed by the LP (red trapezium, Fig. 3). This is supported by the current variability, agreeing to an LP–rod connection of potential while Cassini was in the solar wind close to Saturn (see fig. 2 in Jacobsen et al. 2009). To avoid this variability and to minimize the impact of photoelectrons from the rod, the rod's diameter was made as thin as possible (6.35 mm) and an outer guard shield, held at the same voltage as the probe, was applied to it (Gurnett et al. 2004). Unfortunately, while the instrument can be well-calibrated on Earth, it is impossible to recreate the conditions it will meet on Saturn (e.g. the existence and geometry of the spacecraft, the photoelectrons impact, etc.). As a result, some parameters that can affect the LP measurements are impossible to be calculated or even predicted, hence we need a fuller understanding of the probe operation, and especially the effects of the photoelectrons.

Based on the plasma charge neutrality, we assume a quasi-neutrality between the electrons and the ions in the inner Kronian magnetosphere; in this region the Debye length is adequate small allowing the system to be studied as quasi-neutral—the median Debye length for our study was around 3.5 m. The spacecraft
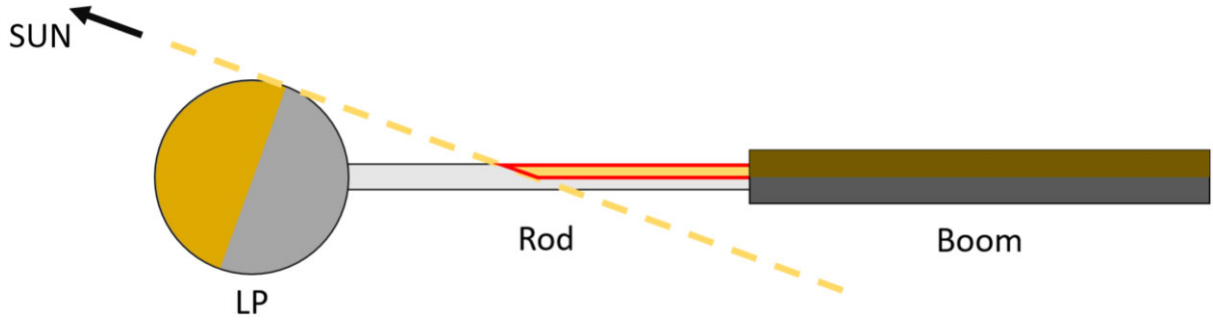
Figure 3. One of the additional parameters affecting the photoelectron generation is the rod connecting the LP with the spacecraft. While the sunlight illuminates half of the probe, the photoelectron current generated from the rod varies, as it depends on the part of the rod that is shadowed by the LP (red trapezium). To avoid this variability and to minimize the photoelectrons impact from the rod, the rod's diameter was made as thin as possible (6.35 mm) and it also has an outer guard shield that is held at the same voltage as probe. Figure adapted from Jacobsen et al. (2009).

charging can also affect the photoelectron current. As the electrons are lighter compared with the ions, they move faster and are associated with a larger charging current. On the other hand, while Cassini is in sunlight, the generated photoelectrons remove some of its negative charge. As the escaping photoemission current is less than the incoming charge from the surrounding plasma the spacecraft is under the negative $U_{s/c}$, where it eventually balances between the incident plasma electrons and photoelectron emission. While Cassini is in an eclipse though, the photoelectron production drops drastically due to the lack of sunlight, making the spacecraft even more negatively charged, throwing that initial balance for both the $U_{s/c}$ and U_{fl} off. There are two ways the LP can be in the shadow: either when Cassini is in an eclipse, or when the spacecraft itself casts its shadow on the instrument. As the periods when the LP is in the spacecraft's shadow are rare—there are only 10 orbits in which the LP was at some point in Cassini's shadow and not all of them have good data—we are mostly focusing on the periods where the spacecraft was eclipsed by Saturn or its rings.

2.2 Searching for eclipses

We found the periods where Cassini goes into Saturn's shadow using the NAIF SPICE toolkit (Acton 1996) function *cspice_gfoclt* (for MATLAB). In total, there were 118 eclipses; 63 partial eclipses, and no annular eclipses. The partial eclipses lasted for a few seconds each and they appeared right before or right after a total eclipse, so it seems that they corresponded to the time Cassini needed to get completely into Saturn's shadow, hence we merged them into the total eclipses.

For each eclipse, we also calculated the 'eclipse depth' which measures how 'deep' Cassini goes into eclipse behind Saturn—a depth of 1 indicates Saturn is exactly between Cassini and the Sun and a depth of 0 indicates that Cassini is not eclipsed. For a vector from Cassini to the Sun we used the *cspice_recpgr* function to calculate the planetographic coordinates of the intersection point with Saturn. We determined the altitude of the intersection point, taking into account the flattening coefficient of the planet (Withers & Jakosky 2016), and obtained a normalized result so if Cassini is in the centre of the eclipse (i.e. the vectors Cassini–Sun and Cassini–Saturn are parallel) the eclipse depth will be equal to 1, while if Cassini is not in eclipse the eclipse depth will be 0.

For calculating the eclipses of the rings, we found intersections of the Cassini–Sun vector on the Kronian equatorial plane, focusing only on times where Cassini was behind Saturn. If the distance in the equator was in between 1.11 and $2.27R_S$, then Cassini was behind the rings, i.e. in the rings' shadow. We also divided that distance to each of the individual major rings: D ($1.11-1.24R_S$), C ($1.24-1.53R_S$), B ($1.53-1.95R_S$), Cassini Division ($1.95-2.03R_S$), and A ($2.03-2.27R_S$) (William 1995). Even though we included the F ring ($2.325-2.335R_S$), it was found that the ring was too narrow to create any observable effects.

In our analysis we focus on two areas: (1) whenever Cassini is in Saturn's shadow and (2) whenever the Cassini is in the ring shadow. Therefore, our data were divided in two categories, based on Cassini's orbit geometry: eclipses by Saturn, and eclipses by both of the bodies. Table 1 shows an overview of the eclipses. We should mention that while Cassini is in Saturn's shadow we ignore any possible rings shadowing, simply because the light is already blocked by the planet.

Table 1. Eclipse summary accompanied with the data description. The LP operates either in a high-resolution rate, or a low-resolution rate. The inconclusive data are orbits either had too sparse data points, or data of low quality.

Description	Number of eclipses of Saturn	Number of overlapping Saturn-rings eclipses	Number of eclipses of rings
High-resolution LP data	11	6	24
Low-resolution LP data	28	5	19
Mixed resolution data	2	–	7
No LP data	11	53	33
Inconclusive data	–	3	5
Total	51	73[a]	88

Note.

[a] Six of the eclipses by the rings were totally in Saturn's shadow (behind the planet), so we are analysing the data type of the rest of the 67 eclipses.
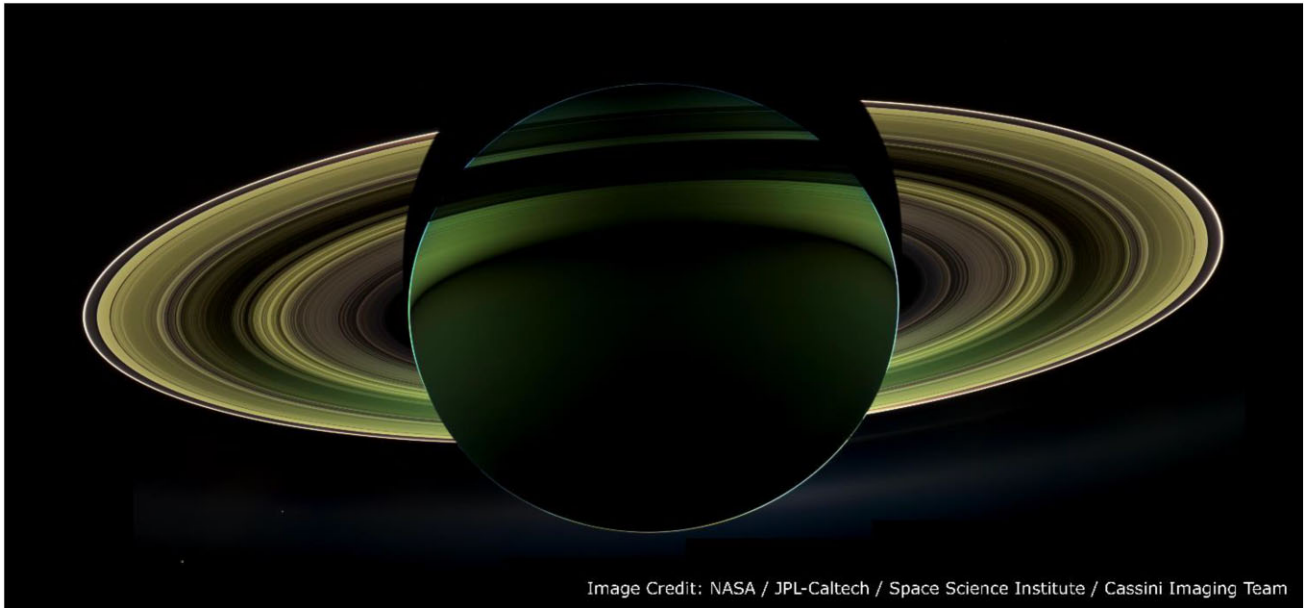
Figure 4. A beautiful view of a solar eclipse from Saturn taken by the Imaging Science Subsystem. The image is a combination of images in the infrared, red, and violet spectral filters. Even if Cassini is in the night side, the shadow of the rings is still visible on the planet. As the rings are highly reflective, they reflect the sunlight even in the shadow of the planet. In our work, we treat the rings as solid, non-reflecting bodies, ignoring any reflected sunlight. Image credit: NASA/JPL-Caltech/Space Science Institute/Cassini Imaging Team.

We must also note following points: (1) The rings can reflect and scatter sunlight in Saturn's shadow, as seen in Fig. 4. In this work, we treat the rings as solid, non-reflecting bodies, ignoring any reflected sunlight. (2) Each orbit has one eclipse by Saturn and/or one eclipse by the rings. During Cassini's Grand Finale in Rev 270–286, Cassini was being shadowed by the rings twice in each orbit, due to the orbit geometry. (3) We did not use any data during the Grand Finale orbits as Cassini was too close to the ionosphere of the planet, resulting to data we could not use for the purposes of this study.

Overall, we found 118 solar eclipses by Saturn, and 161 solar eclipses by Saturn's rings. In 73 instances there was an overlap of the eclipses caused by the two bodies: In six occasions the eclipse by the rings was totally in Saturn's shadow, while in 67 occasions Cassini was already in the ring's shadow while entering Saturn's shadow, or vice-versa; an example of each case is presented in Fig. 5. We also present an overview of the eclipses with the type of the available data (high-resolution, low-resolution, mixed, and no data) in Table 1. A table with the full details for each eclipse can be found in Appendix A.

3. OVERVIEW OF DATA DURING ECLIPSE AND RING SHADOWS

Fig. 6 shows an example of the LP data during a ring shadow and eclipse event. It is focused on an eclipse during rev. 046 and it is the 12th eclipse by Saturn in our data set, with a duration of 119 min. The top three plots show Cassini's orbit in KSMAG (the unit vector of the z-axis, e_z, is pointing along the Kronian magnetic dipole axis, $e_y = e_z \times e_{sun}$, and e_x lies in the Kronian equator completing the right-handed orthogonal system) also following the location of the Sun (time goes from blue to red), while the middle plot shows the LP spectrogram and calculated electron densities and temperatures, along with the location of Cassini and the eclipse depth.

The spectrogram shows the measured current as a function of bias voltage and time where the magnitude of the current is shown in the colourbar. The horizontal lines around −3 and −17 V are caused by interference from another instrument. A notable feature on the spectrum is the change of the spectrum when Cassini enters into a body's shadow, where the ion current almost reaches the noise level. An example of this is shown at the sweeps at the bottom of Fig. 6: The sweep on the left is when Cassini is not in an eclipse, and on the right is when Cassini is in an eclipse. The upper panel is the I–V curve in linear scale while the bottom panel is the magnitude of the current on a logarithmic scale. The change in the ion current between the two examples is clear: The ion current outside the eclipse is around −1 nA, while inside an eclipse is less than ±100 pA, which is the threshold of the electronic noise of the instrument. This change is connected to the lack of photoemission while Cassini is in the shadow. The ion-side current is the sum of the photoemission current and the ion ram current (the cold plasma electrons do not contribute here as they are repelled due to the negative bias voltage this region). Hence, as the current from the plasma electrons drops to near zero on the ion side, the ram ion current is very small, and the photoemission goes to near zero, the ion-side current is a near-zero current during the eclipses. Also, another noticeable feature between the examples is that the floating potential is clearly identified by the inflection in the current magnitude when Cassini is outside of an eclipse, while it is not clearly noticeable inside in an eclipse.

As Cassini passes through the shadow region of each ring—identified by the bars at the top of the figure—we can see that each ring has a different signature. The A and B rings show similar behaviour as Cassini being eclipsed by Saturn, with the ion current dropping to zero, while C and D rings are modified very little compared with before going into the A ring. Focusing on the A, B, and C rings, we see that all three show some kind of structure on the ion current. The A ring has the more intense changes, as in some regions that the ion current drops to zero, while in others the spectrum looks very similar to that being outside the shadow. The B
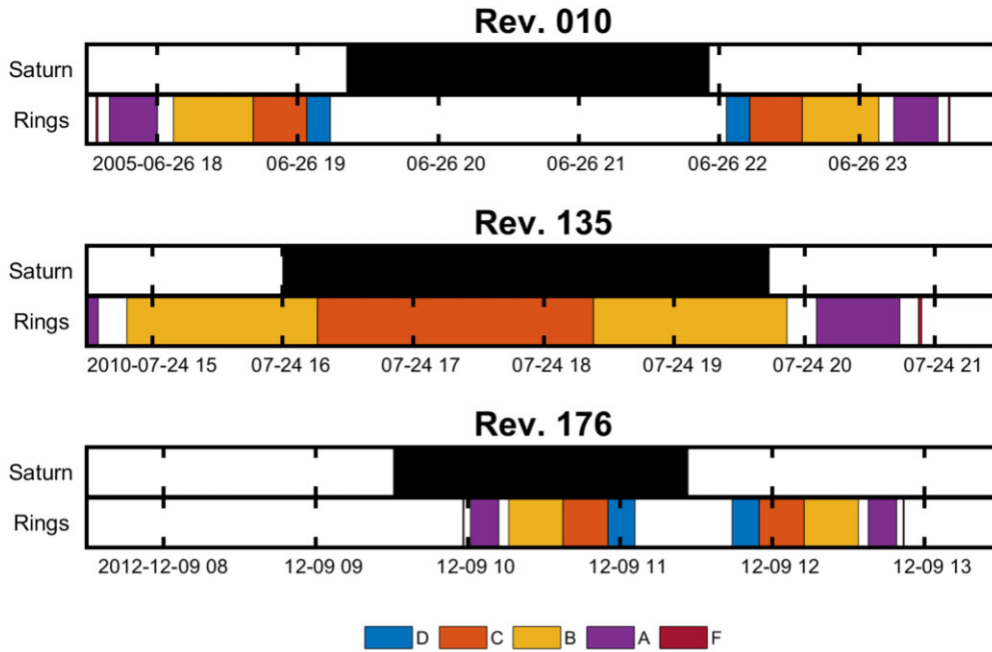
Figure 5. Schematic of the three cases between eclipses by Saturn and the rings. The first panel shows a case when the eclipse by the two bodies completely separated (rev. 010 example), the second panel shows a case where the eclipse by Saturn occurs during an ongoing eclipse by the rings (rev. 135 example), and the third panel shows a 'hidden' eclipse of the rings that occurred during an on-going eclipse by Saturn (rev. 176 example).

ring has more subtle changes, with the ion current on the outer inner B ring to be more time closer to zero than that on the inner B ring. Lastly, there are some subtle changes on the ion current intensity in the middle the C ring.

Another interesting feature is how the number of electron populations varies during the periods where Cassini going into an eclipse or exiting from it (fourth panel of Fig. 6). As we mentioned in Section 2, the electron plasma can be expressed by the best fit of a multiple electron population model; the total electron density is the sum of the density of the individual populations. In the example, we see that before it goes into an eclipse we require a three-population electron plasma density; however, as it goes into the A ring shadow it drops to only one-population, which holds in the B ring shadow. As it enters the shadow of the C ring, then there is a re-appearance of a second population, which it stays in the D ring shadow, and eventually disappears when it enters Saturn's shadow. In the middle of the eclipse a second population appears, and a third one appears before the end of the eclipse. While the population number change is consistent with one of the populations being the photoelectrons—that disappear when Cassini passes behind optically thick rings or enters Saturn's shadow—it does not explain the appearance of the second population during the eclipse or the third population before the ending of the eclipse. Additional parameters have to be taken into consideration, like the density radial and spatial distribution (based on Persoon et al. 2020 showing in the dashed green line), also possibly the geometry and orientation of Cassini, or even use fittings with additional electron populations models.

Lastly, an additional feature that should be mentioned is the increase on the ion current towards the ending of the eclipse around 22:30 UT. This could denote that Cassini went into a region of energetic electron plasma where scattered sunlight generated photoelectrons, or the ion current is becoming more important, as Cassini is seemingly moving into a higher density region. This is an isolated example, as most of the orbits do not have an asymmetrical

spectrum during an eclipse by Saturn. We speculate that this increase is a result of Cassini entering a region of energetic electrons, but as we mentioned earlier we are confident that these events are rare in our analysis.

While we presented a good-looking example of an eclipse by Saturn, we must note that not all of our examples are that well-structured. Such an example can be seen on Fig. 7, for eclipse number 46 during Rev. 133., where, while the LP spectrum still changes when entering Saturn's shadow, the change is not as clear or consistent as the example in Fig. 6. While in eclipse the negative bias current gets close to zero, but it does not cross it, opposed to the example in Fig. 6—this could be a result of Cassini being in a high-density plasma, where the ion current is higher than the instrument thermal noise, hence it is non-negligible. Additionally, there is no change in the number of electron populations when entering the shadow, and the appearance of the third population happens before the ending of the eclipse. There are about 20 eclipses of this type.

4. RING SYSTEM OPACITY IN EUV

In Section 2, we mentioned that when the LP is negatively charged, the measured current, I_-, is the sum of the ion ram current I_i, the photoelectron current, I_{ph}, and the secondary electron current $I_{sec.e}$. In Section 3, we saw that the I_- changes dramatically when Cassini enters the shadow (example in Fig. 6); this is something that was observed–and expected–in every eclipse. Since the change in current was very rapid compared with the motion of the spacecraft, this cannot be caused by a change in the surrounding ion density, or the secondary electron current, as the energetic ions/electrons impact rates are usually negligible in these regions (e.g. Thomsen et al. 2016). That leaves us with the photoelectron current to be the driving force of the change in I_-.

Focusing on the LP spectrum of each ring (as seen in example in Fig. 6), we see that there are some differences between them—as
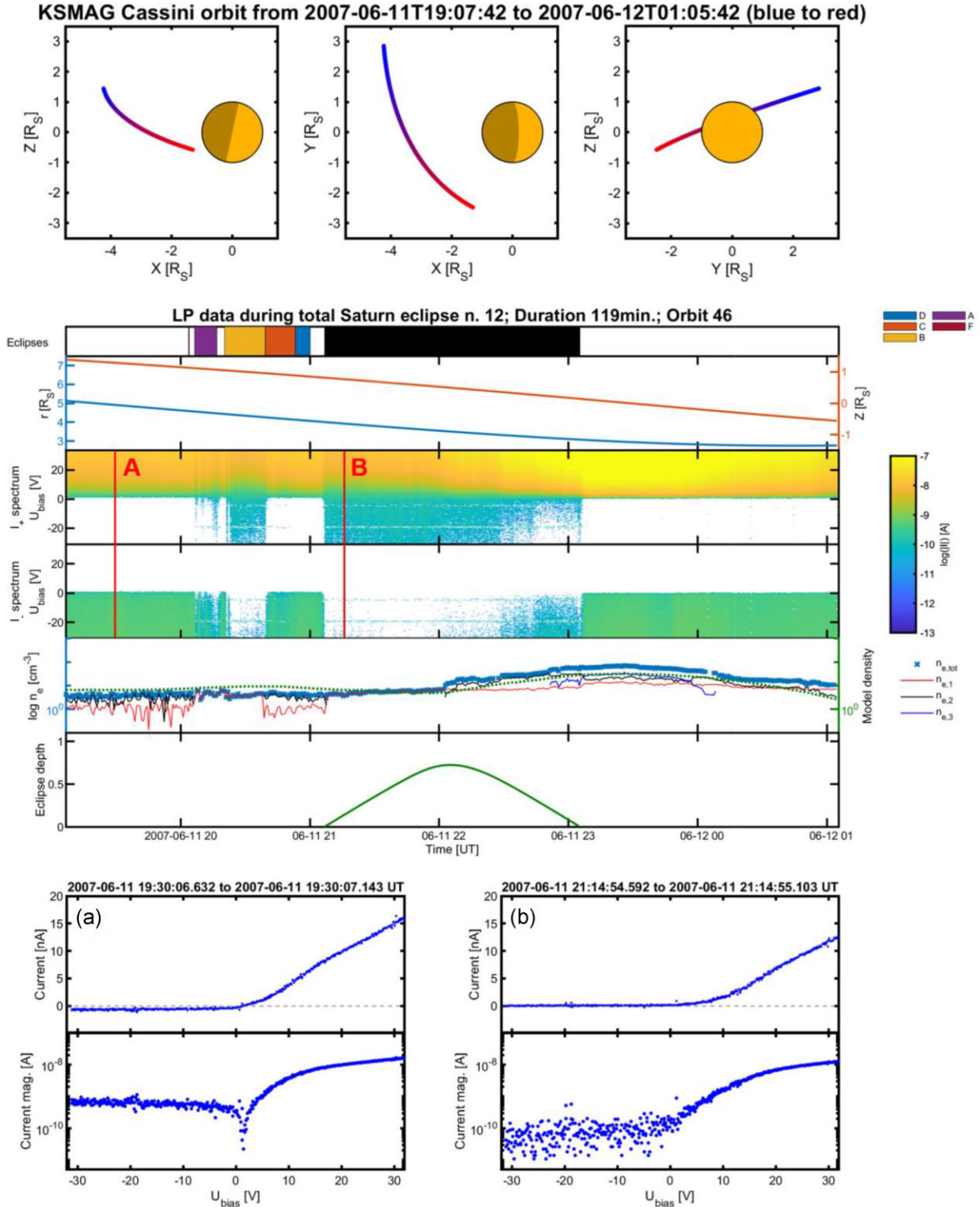
Figure 6. Geometry and data for the Rev 46 eclipse observations. The top panels show Cassini's position in KSMAG (time goes from blue to red). The time-series data in the bottom panels show the data with colour-coded eclipses by the rings and planet at the top of the figure. The data panels show (1) the radial distance (blue) and vertical distance from the equator (orange), (2) and (3) show the LP I–V spectrogram (for positive currents and negative currents, respectively), (4) the calculated electron density (blue points) with the corresponding fitted populations (red, black, and blue lines), and the magnetospheric electron density model (green dashed line) (by Persoon et al. 2020), (5) the eclipse depth (green solid line). The two I–V curves on the bottom correspond to the markers A and B in the LP spectrum.
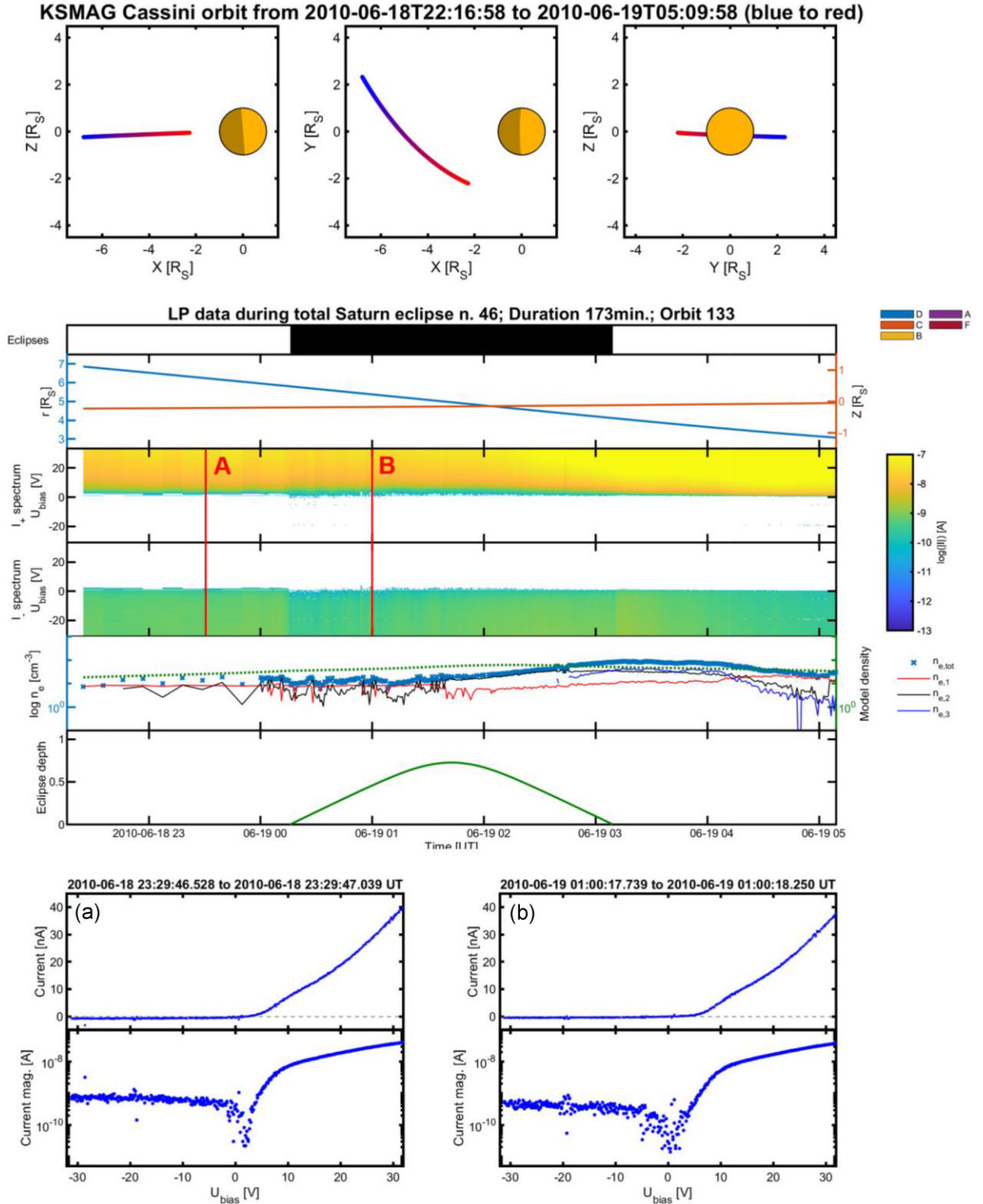
Figure 7. Time-series plot showing the eclipse by Saturn during rev. 133 (same panels description as in Fig. 6).

an example we set a comparison of Cassini going in the shadows of the B ring and the C ring: While the current for the entire range of bias voltages was constantly positive for the B ring, for the C ring it was positive in the negative bias voltages and negative in the positive bias voltages. The difference in those measurements could be linked with the difference in the optical depth in the EUV part of the spectrum of the rings (as this is the region of the spectrum that generates photoemission).

In general, the optical depth is defined as the ratio of the incident radiant flux, Φ_e^i, to the transmitted radiant flux Φ_e^t:

$$\tau = \ln \frac{\Phi_e^i}{\Phi_e^t} \tag{7}$$

where the radiant flux is a wavelength integral of the spectral radiant flux, $\Phi_{e,\lambda}$ (McCluney 2014)

$$\Phi_e = \int_0^\infty \Phi_{e,\lambda} \mathrm{d}\lambda. \tag{8}$$

We can use the LP photoemission current as a proxy for radiant intensity: When the sunlight passes through a material, part of it can be absorbed or scattered, hence its intensity will get reduced, and the number of photoelectrons that will be generated at the probe will decrease. A more detailed description of the how the LP currents can be used as a proxy for the radiant intensity is presented in Appendix B but we define the optical depth (equation 7) in terms of the photoemission current as

$$\tau = \ln \frac{\Phi_e^i}{\Phi_e^t} = \ln \frac{I_{\mathrm{pe}}^i}{I_{\mathrm{pe}}^t}. \tag{9}$$

While from a mathematical perspective the optical depth is somewhat straight-forward to be defined, we must take into consideration two additional factors when we try to calculate the optical depth of Saturn's rings: The Sun–Cassini–rings plane angle, and self-gravity wakes in the rings. The first factor, the angle between the Sun–Cassini–rings plane can be expressed as a normalization 'viewing factor', linked to the path of the sunlight through the rings and correcting the distance the sunlight travelled through the rings to give the normal optical depth. As that distance depends on the angle it enters the ring plane, the viewing factor, ξ, was defined as the cosine of between Cassini and normal plane vector with respect to the equator; a graphic representation of the angle (projected in two dimensions) is presented in Fig. 8, where $\xi = \cos\theta$. The minimum and maximum values of the viewing factor depend on the incident sunlight, connected with Saturn's inclination on the orbital plane, that is $26.73°$. At Saturn's equinoxes the sunlight comes parallel to the ring plane, hence the angle θ is on its maximum value $\theta_{\max} = 90°$ and the viewing factor has its minimum value $\xi_{\min} = 0$. On the solstices though the incident sunlight angle is at $26.73°$, the angle θ takes its minimum value $\theta = 63.27°$, and the viewing factor takes its maximum value $\xi_{\max} \approx 0.45$. Fig. 8 also shows how the incident and transmitted currents (from equation 9) are defined and where they are measured over a specific distance ρ. Our data set could be divided in four angle groups: data points with the sun being in angles smaller than $72°$, between $75°$ and $79°$, between $80°$ and $83°$, and over $84°$.

The second factor, the self-gravity wakes, has to do with the structure of the A and B rings. The self-gravity of the ring particles creates azimuthal density wakes (Colombo et al. 1976) grouping ring particles into bars with space in-between, which have been observed in various wavelengths (e.g. Dunn et al. 2004; Nicholson et al. 2005). No self-gravity wakes have been observed in the C and D rings. There are two main models calculating the optical depth of the A and B rings, each using data of a different instrument. The 'Granola Bar' model (Colwell et al. 2006) describes the wakes as infinitely long rectangular slabs, and was developed using data from the Cassini's UVIS, and (as Jerousek et al. 2016 said 'in keeping the culinary naming theme') the 'Pasta' model (Hedman et al. 2007) describes the wakes as infinitely long opaque tubes with ellipsoidal cross-section, and was developed with the help of Cassini's VIMS. Both models are parametrized by similar physical properties of the wakes: The 'Granola Bar' model (Colwell et al. 2006, 2007) uses the ratios
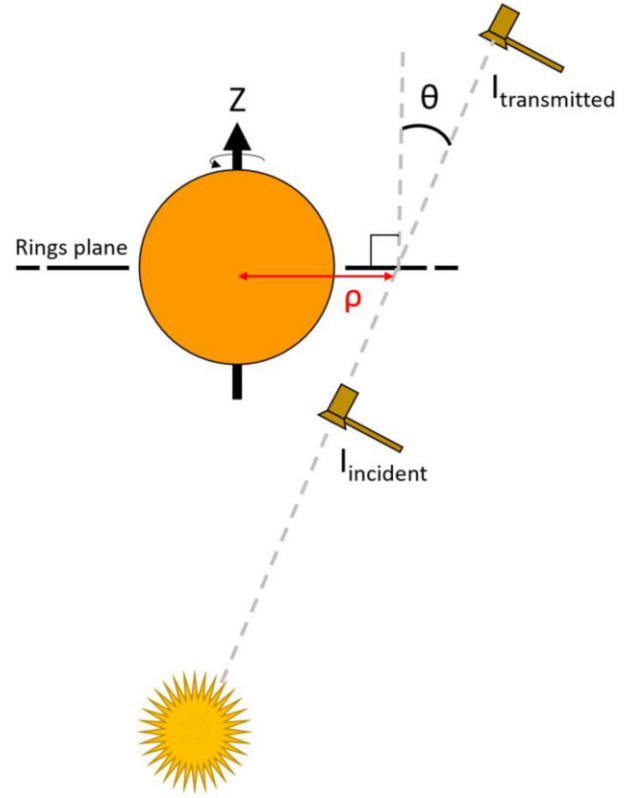

Figure 8. A graphic representation of the transmitted and incident currents, and the normalization angle.

of the height (H) and separation (S) of the wakes with respect to their width (W), H/W, and S/W, the orientation of the wake, φ_w, and the optical depth of the gaps and the wakes, τ_G and τ_w, respectively, while the 'Pasta' model (Nicholson & Hedman 2010) uses the separation (G) and height (H) of the wakes to their characteristic wavelength, λ, i.e. the distance of the width (W) of the wake and a separation between them ($\lambda = G + W$), G/λ and H/λ, and the optical depth of the gaps, τ_G. In the limit where the angle θ is almost 90 degrees, i.e. the source and the observer are almost parallel to the rings plane, the two models 'collapse' to the same result.

The results of the two models are difficult to compare for two reasons: due to the differences in the assumed geometry of the wakes, and due to VIMS and UVIS operating in different wavelengths. Jerousek et al. (2016) combined UVIS and VIMS measurements and used a modified self-gravity wake model, and they found that the structure of the wakes is different in the two rings: In the A ring, the wakes are clearly separated with relatively empty gaps between them, and an optical depth of ~ 0.1, while for the B rings the gaps are not that well-defined, and their optical depth is higher. They also found that the angle θ is playing a bigger role on calculating the optical depth than the observing wavelength.

For this study, for the A and B rings we are using Colwell et al. (2007) model with the Jerousek et al. (2016) parameters, that took into account the observations from both UVIS and VIMS, while for the C and D rings we are simply correcting the light path using the viewing factor, ξ, as defined above:

$$\tau_n = \begin{cases} \tau_G - \ln\left(\dfrac{S/W - H/W\ |\sin(\varphi-\varphi_w)|\ cot(90-\theta)}{S/W + 1}\right)\xi & A, B\ rings \\ \tau_G\xi & C, D\ rings \end{cases} \tag{10}$$

Table 2. Values of the S/W and H/W parameters for each of the regions of the B ring based on visual averages of the data in Fig. 8 of Jerousek et al. (2016).

Region	S/W	H/W
B1	1.125	0.1
B2	0.188	0.038
B3	0.094	0
B4	0.125	0.019
B5	1.125	0.15

where H/W and S/W are the height and separation of the wakes with respect to the width of the wake, φ is the prograde angle between the projection to the equatorial level of the Cassini–Sun light of sight and the local radial direction, and φ_{w} is the orientation of the wake; for a more detailed view of the geometry see fig. 2 in Jerousek et al. (2016).

The values of S/W and H/W, presented in Table 2, were calculated from Jerousek et al. (2016). For the A ring we fitted a linear fit on the model values (see their fig. 7) over the radial distance, ρ, getting the equations $S/W = 0.751\rho - 1.421$ and $H/W = 8.035\rho - 15.703$, and for the B ring (see their fig. 8) we took the average of each region:

Of course we acknowledge that this is not the most accurate method in obtaining the values of the parameters. To evaluate the impact of this we recalculated the analysis for B1, where the S/W values varied the most, using some extreme values 0.5 and 1.5. Between these extremes the opacity changed by about 10 per cent, while for more modest variations in S/W the opacity changed by about 5 per cent, which is well within the statistical variation of our sample as we will show later (Fig. 11). Therefore for the purposes of this study this approximation is adequate.

The values of φ_{w} differ not only between the two rings, but also on the method of observation: For the B ring, Colwell et al. (2007) calculated a range of $69°-90°$; while for the A ring, Salo, Karjalainen & French (2004) using numerical simulations calculated an angle of $\sim 69°$, Hedman et al. (2007) using VIMS observations calculated an angle of $63°-73°$, Colwell et al. (2007) using UVIS calculated an angle of $45°-80°$, and Ferrari et al. (2009) using thermal emissivity variations calculated an angle of $\sim 70°$. For our work, we use $\varphi_{\mathrm{w}} = 70°$.

We chose to use the median of the current around $U_{\mathrm{bias}} = -11$ V (between -8 and -14 V bias voltages) as that specific bias voltage was far from any interference of other instruments (mentioned in Section 3); we also took the median rather than the average in order to overlook any extreme values due to random noise/interference from other instruments. Also, for this part of the study, we limited our data set to the period where Cassini was in the rings' shadow, but not in Saturn's shadow.

We also investigated any possible errors that would have been introduced from Cassini's movement during a sweep. The LP needs 46 ms to measure the current between -8 and -14 V, in which Cassini moved a maximum of about 950 m; this is the theoretical minimum limit for detecting any structures on the rings, i.e. any structures smaller than 950 m cannot be resolved no matter how many data points we have. In practice, though we also need to consider additionally: the sample rate of the LP and the sample size of our radial distribution. As mentioned in Section 2, the sample rate of the LP, depending on the operation mode, is 10 min or 10 s. During this time, Cassini moves about 13 000 or 210 km, respectively. Therefore, if we only had a single orbit, the spatial

resolution would have been limited to those distances. As we have data from multiple orbits, we have a larger sample size which improves our spatial resolution. As the reader will ultimately see, the average radial resolution for our study is around 1000 km. This of course depends on the number of data points for each radial distance from Saturn, e.g. some bins in B1 are narrower than those in B3.

Fig. 9 shows the current over the distance the Cassini–Sun vector intersects Saturn's equator. To statistically analyse the measurements we binned the data by distance from Saturn in the ring plane. The bins were generated by recursively subdividing the spatial range into smaller and smaller bins until the 1331 measurements were distributed with a minimum of 20 data points per bin. This gives us the best spatial resolution whilst maintaining a statistically meaningful number of data points in a bin. Subdividing to a smaller number of data points, e.g. 10 or 15, provided a higher resolution and allowed us to see more structure, e.g. to partially resolve the Colombo gap, but it also introduced more scatter, therefore we used a minimum of 20 points.

Similar to that deduced from an analysis of Fig. 6, from Fig. 9 we can see that the measured current is different over each ring. Over the A and B rings the current is almost at the noise level. Over the D ring the current is essentially indistinguishable from the background. Over the C ring the current is intermediate between the A/B rings and the C ring. As discussed in Section 3, when the negative bias current is close to the noise level there is negligible photoemission and so we can conclude that the A and B rings are the most optically thick; the B ring is the most optically thick since the current is closest to the noise level. The D ring is the least optically thick and the C ring is intermediate between these extrema. The individual zones within the B ring are not clearly identifiable in Fig. 9, although there is a drop from part-way through B4, through B5 to the Cassini Division that could be indicative of changing opacity in this region, but we are not able to say more due to the small number of data points in this region.

The largest of the ring gaps (Maxwell and Encke) are clearly identifiable as inflections in the measured current at those locations. There are hints of the Colombo gap in the raw data but following our binning procedure this gap is not resolvable due to the number of points in this region and the resulting coarse bin size at this location. For similar reasoning, we are not able to make any statements about the F ring.

In order to estimate the incident sunlight (numerator in equation 9), we calculated the extension of the Sun–Cassini vector while Cassini was between Saturn and the Sun (see Fig. 8 for a graphic representation of the position of Cassini for these measurements). Our sample was 2562 data points that we recursively subdivided into bins with a minimum of 20 data points per bin. Fig. 10 shows this current over the radial distance; the parameters for Fig. 10 are identical to those of Fig. 9. On the upper plot, one can distinguish two groups of measurements: once closer to 0, and one closer to -0.5 μA. The near-zero measurements are from Cassini's Rev. 249 (day 320/2016 to day 328/2016) and 253–259 (day 350/2016 to day 34/2017) and the origin for these anomalously low currents is not clear. Potential reasons could be the change of the instrument's operation during Cassini's mission in 2008 August), or Cassini being in larger L-shells, where the ion current is negligible and the negative-bias current is just photoemission.

As seen in Fig. 10, the current is almost constant in radial distance with a mean value of $\overline{I_{\mathrm{inc.}}} = -0.4471$ μA and a standard deviation of $\sigma_{I_{\mathrm{inc.}}} = 0.022$ μA. We can calculate the uncertainty in the current with the standard error, $a_{I_{\mathrm{inc.}}} = 0.00253$ μA. Hence the current from the incident light is $\overline{I_{\mathrm{inc.}}} = -0.447 \pm 0.003$ μA. We argue though that
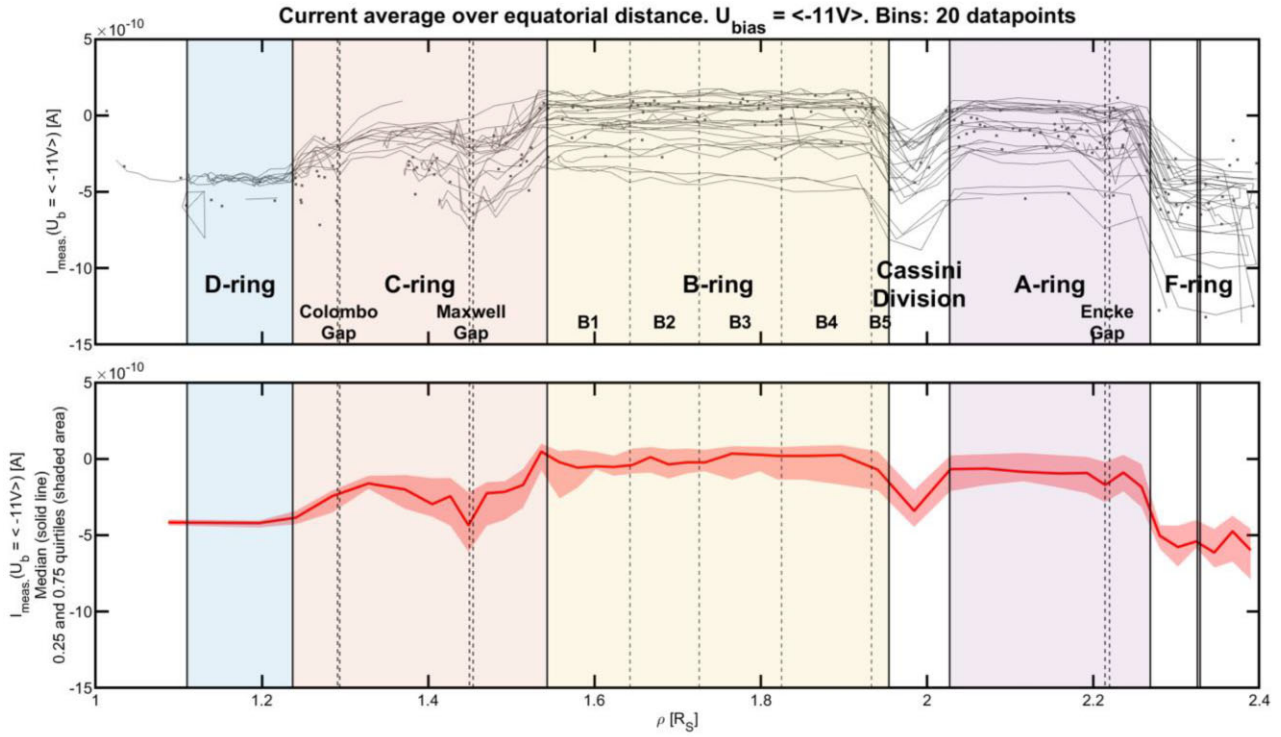
Figure 9. The measured current around $U_{bias} = -11$ V over the Kronian equatorial distance. Top panel: Raw data (lines show continuous sets of measurements; points show point measurements). Bottom panel: Median (solid line) and the 0.25 and 0.75 quartiles (shaded area). The coloured areas show each ring and the dashed lines show some features of the rings: the gaps, or the regions of the B ring.
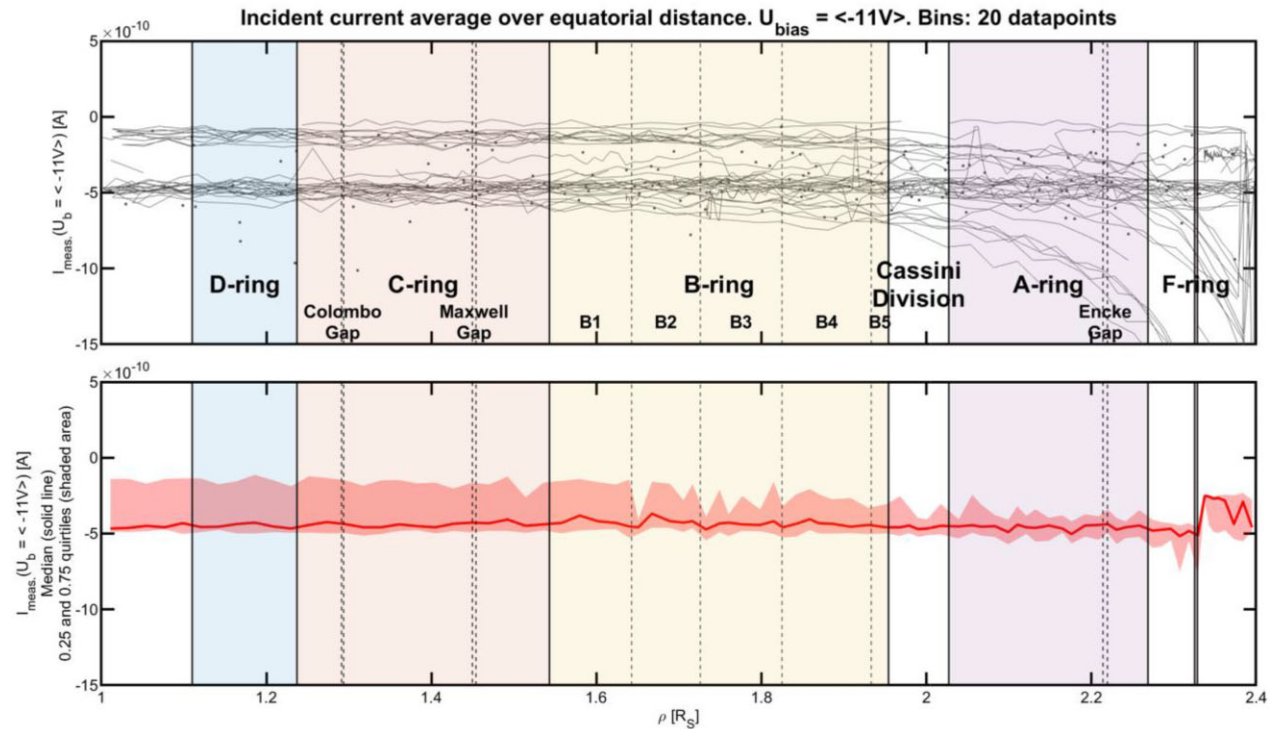

Figure 10. The measured current around $U_{bias} = -11$ V over the Kronian equatorial distance when Cassini was in-between Saturn and the Sun. The figure is in a similar format to Fig. 9. Top panel: Raw data. Bottom panel: Median (solid line) and the 0.25 and 0.75 quartiles (shaded area).
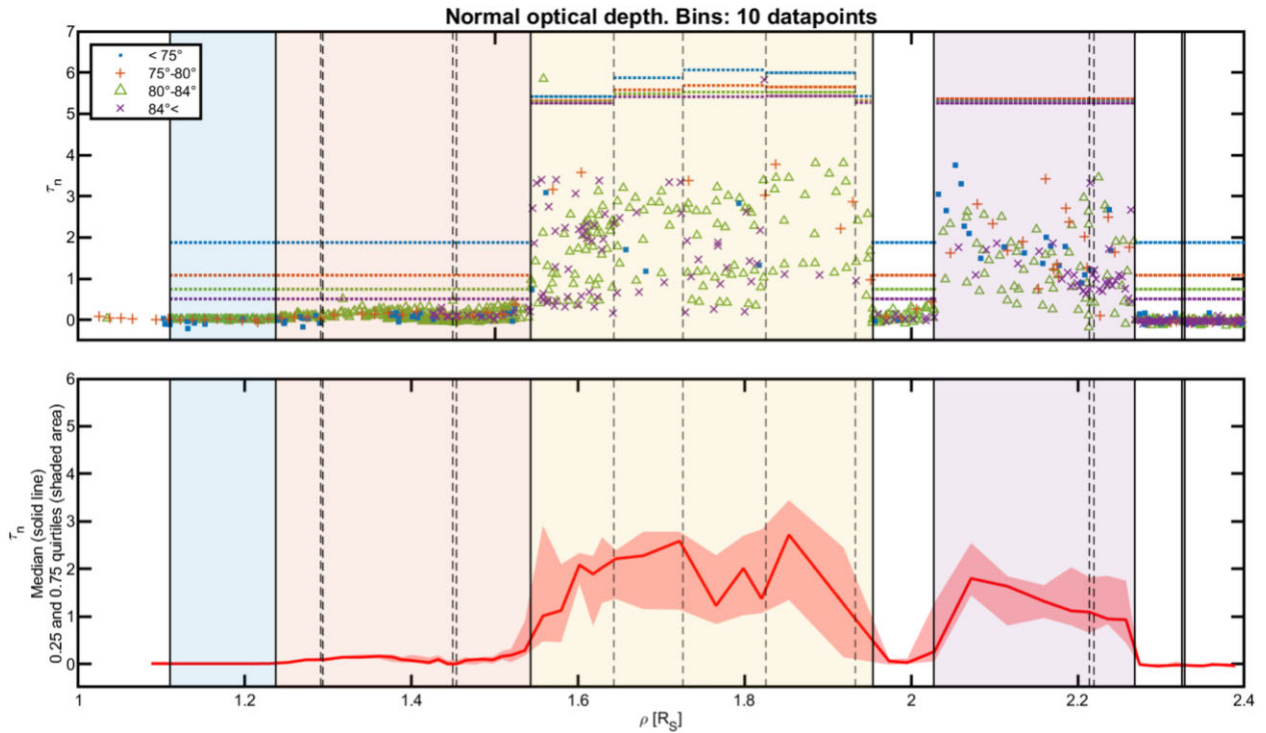
Figure 11. Normal optical depth for our data set, after all the factors have been taken into consideration. Top panel: Raw data, divided into four angle groups, colour-coded, based on the legend on the top right. The symbols show the data points where the logarithm was positive, while the dashed line shows the maximum optical depth, τ_{max}, for that group. Bottom panel: The median of the positive data points (red line) with the corresponding 0.25 and 0.75 quartiles (shaded area)—similar to bottom of Fig. 9.

our statistical analysis will not be affected from the differentiation between the two groups of the incident current (one close to 0 and one close to -0.5 μA) as, even though there was a big difference between the 0.25 and 0.75 quartiles, the standard error narrowed down the uncertainty.

Based on equation (11), we can define the optical depth for each of the data points simply by calculating the natural logarithm of the ratio the incident current to transmitted current ratio, plus the added factor for A and B rings. Here though we are facing a problem: While the incident current is negative, some of the transmitted current is positive, making the ratio negative, whose natural logarithm cannot be defined. The main reason for the positive data points is the random electronic noise, a possible interference by other instruments but also the change of the spacecraft charge—even if we tried to avoid it in the best possible way. In order to solve that issue, we followed a method similar to Colwell et al. (2010), where they defined a maximum optical depth, τ_{max}, based on the minimum number of counts they could measure. For our case the minimum current corresponds to the noise level of 100 pA so we set the minimum measurable current to be the standard error of our measurement of the incident current. Hence, the maximum optical depth we get from our measurements is

$$\tau_{max} = \ln \frac{I_i}{a_{I_i}}. \tag{11}$$

The top panel of Fig. 11 shows the optical depth for all the data points based on equations (10) and (11), i.e. taking into consideration all the factors we mentioned earlier: the angle of the sun, the statistical maximum depth, and the correction for the A and B rings self-gravity wakes. Each colour is linked to an angle group shown on the legend on the top right. All data in an angle of smaller than 75° are in blue dots, between 75° and 80° are in orange

crosses, between 80° and 84° are in green triangles, and over 84° are in purple x's. The dashed lines show the maximum optical depth, τ_{max}, for the group of the specific colour. The lower panel of the figure shows the median of the positive data points (red line) with the corresponding 0.25 and 0.75 quartiles (shaded area).

The correction introduced from the inner B ring to the end of the A ring increased dramatically the optical depth of the region compared with the C and D rings. The normal optical depth of the D ring is very close to 0, while for the C ring is around 0.1. It worth mentioning that the Maxwell Gap is visible in our measurements, as the optical depth falls close to 0, i.e. there is not that much absorbent matter in the area; the Colombo Gap though was not visible. The normal optical depth of the B ring is the highest of all, with its median varying from over one to almost two, and lastly the A ring dropped from under two (inner edge) to around one (outer edge). The Encke Gap was not as clear as in Fig. 9, but we estimate that this is a result of the binning: Even though we binned the data in 10-data points bins to maximize the resolution without losing information, it seems that the bin was simply too big and it just smoothed out the Encke Gap. Also, the couple data points that seemingly are over τ_{max} are safe to assume that they are not real: This can happen when the value of the data point is positive, but smaller than the statistical error of the measurements, used for equation (11).

5. DISCUSSION AND CONCLUSIONS

5.1 Main results and limitations

For our study we studied the changes of the LP connected with the periods that Cassini goes into the shadow of Saturn or its rings. As Cassini enters into the shadow, the illumination from sunlight

drops dramatically and photoemission drops accordingly. Taking into consideration the photoelectron yield of the LP and the structure of the rings themselves, we calculated the optical depth across the rings and we found that the most EUV-opaque ring is the B ring, followed by the A ring, the C ring, and lastly the D ring that was almost transparent. We also managed to observe the major gaps of the rings: the Maxwell Gap in C ring and the Encke gap in A ring. The Colombo Gap was observable on some individual orbits, but due to the small number of data points around the distance of the gap it was lost in the averaging process. Cassini moves about 1 km during the measurements of each data point, so we argue that this represents the absolute minimum spatial resolution for these measurements.

The LP is sensitive in the EUV wavelengths–mainly the Lyman-α line, with some contributions from shorter wavelengths–hence our results can be compared with those of Esposito et al. (1983) and Colwell et al. (2006, 2007, 2010), where they also calculated the optical depth in the UV-C (the first study) and EUV (the rest studies) part of the electromagnetic spectrum and our results are in good agreement. The optical depth we calculated for the D ring is very close to 0 and for the C ring it was ~ 0.1, which both agree with previous studies. For the B1 region, our calculations showed an increasing optical depth to ~ 2, while in previous studies it was around ~ 1, for B2 our calculation of ~ 2 agrees with the previous studies, and for B3 we calculated ~ 1.5, where previous studies calculated it to be ≥ 2. While for B4 we had a drop from ~ 2 to ~ 1 as the distance increases, which did not agree with values of ≥ 2 of previous studies, we estimate that the small number of data points in this region does allow us to extract a safe result—same for B5, where we had a few data points ~ 1.75 while previous studies had a significantly greater optical depth of over two, or even around three. For the Cassini Division, we calculated an optical depth of ~ 0.1, which agrees with previous studies. Lastly, for the A ring, our values were a bit higher than past studies: ~ 1 compared with ~ 0.5.

We estimate that the main reasons for the discrepancies are as follows:

(i) The limited data set of our study compared with the previous studies. We had only 2200 data points compared with tens of thousands of Colwell et al. (2010) for example, and that did not give us a high-enough resolution radially compared with the rest of the studies

(ii) High-energy electrons that impact the LP will generate secondary electrons that are not accounted for in our study. Our measurements are mostly inside the reported mean $L = 6.2$ boundary for energetic electrons (Thomsen et al. 2016) so we estimate that their impact will be minimal. But this may affect some measurements and should be investigated in future studies.

(iii) The rings are mainly made of ice, a highly reflective material, but also have fine structures—e.g. the self-gravitational wakes for the A and B rings (Colwell et al. 2006, 2007). Sunlight can be reflected and/or diffracted, reaching Cassini from areas that are not on Cassini's line of sight with the Sun, generating extra photoelectrons (example of Fig. 4). Also, while in our analysis we took into consideration the self-gravitational wakes for the A and B rings, Colwell et al. (2021) have reported non-axisymmetric narrow features, named 'phantoms', in the regions B2 and B3, with a width of just 10 m. Even if these 'phantoms' width is much smaller than our theoretical minimum location error of around 1 km, they could potentially affect our work as the light will behave the same way it does with the self-gravitational wakes. This feature could potentially help in defining the optical depth of the B3 region—a region that many studies struggle with due to the lack of data.

(iv) Saturn's Planetary Period Oscillations (PPOs). It was found that the PPOs affect the Kronian system [e.g. on the ionospheric diffusive layer modulation (Provan et al. 2021), at the Saturn Kilometric Radiation low-frequency extension events (Bradely et al. 2020 etc.)], hence it is worth studying any possible connection of the fluctuation of the magnetospheric plasma density or appearance/disappearance of the electron populations with the PPOs. In addition, works that argue for an electron density asymmetry, e.g. Gurnett et al. (2007), need to be taken into consideration.

During the data analysis we observed changes in the LP behaviour when Cassini gets into an eclipse, where the negative-bias current, I_-, is drawn towards zero from its 'usual' negative value when it is out of the eclipse. As I_- is the sum of the ion and the photoelectron currents, the change shows that the dominant negative-bias current is the photoelectron current. The reason I_- was usually surpassing zero is not fully understood, but we argue that the three main reasons are: the random thermal noise, Cassini being in a region of high plasma density hence the ion current is not negligible, and the high-energy electrons that manage to overpass the potential and collide with the LP. There are only a few cases when the negative-bias current is not surpassing zero (example in Fig. 7), but regardless if it was surpassing zero or not it was within the noise level, so we feel confident that our results are not compromised by those cases.

5.2 Photoelectrons and analysis of LP data in eclipse

The methodology of Fahleson (1967) for calculating the ion parameters uses a slightly negative spacecraft potential, but during eclipses the spacecraft potential is expected to become very negative, hence the LP data during the eclipses might need to be recalibrated. This does not mean that all the previous studies that used LP data need to be revised: the LP data base has almost 77 000 data points for the entire mission, out of which Cassini was in the shadow of Saturn or its rings in only 4215 of them (2263 for the rings and 1952 for Saturn)—i.e. about 0.5 per cent of the entire data base. Moreover, we do not know how negative the spacecraft potential will become during the eclipses, making it hard to take that factor into consideration for our analysis.

Even though the photoemission current stops when Cassini enters into an eclipse–and begins when it exits from an eclipse–we did not see any consistent change on the number of electron populations: While there were some occasions that a population appears or disappears close to when Cassini enters/exits a Saturn eclipse or an eclipse by the optically thick rings, in the vast majority of the Saturn's shadow crossings or crossings between the rings there was no change in the population number. This could possibly denote that the photoelectrons are not tied to a specific population. We must mention that the cold electron number density changes spatially around Saturn, as shown in Persoon et al. (2020), which could affect the change of the populations number

It is almost impossible to study the LP photoemission and photoelectron current while the instrument is in shadow but the spacecraft is in sunlight, as Cassini's design gave the LP the unfortunate position of being directly opposite the radiators for the VIMS and composite infrared spectrometer (Matson, Spilker & Lebreton 2002). Since the radiators needed to be shielded from the sunlight that meant that the LP would have been constantly in the sunlight. There were only 10 occasions where the LP was in Cassini's shadow and not all of them had useable data. There are also many instances that the LP operation was switched from HR mode to a LR mode for the duration of the eclipse for the necessities of other instruments. This resulted to a

series of eclipses to be practically unusable for us, as there was not a clear passing from the light to the darkness and vice-versa.

5.3 Future work

Future work for this project would be the study the impact of: the high-energy electrons, the secondary electrons, and diffraction or reflection effects. Those factors can potentially change the electron density from 'artificial' sources, electrons introduced by the instrument or the spacecraft, hence they must be taken into account and addressed while studying the ambient plasma. A study of the Cassini parameters and conditions (location, plasma density, etc.) when the negative negative-bias current, I_-, surpasses zero during eclipses would provide us a deeper understanding of the instrument operation. It was also mentioned that the PPOs affect the Kronian system, hence a possible connection of PPOs with either the plasma density fluctuations or the appearance/disappearance of electron populations could be studied. As there are orbits with discrepancies between each other, a study using data from other Cassini instruments that have the capability to measure the cold electron plasma, CAPS or RPWS, could be beneficial to determine the nature and source those discrepancies. Lastly, it also worth investigating the idea of a 'relaxation time' of the photoelectrons cloud, readjusting to any changes in the spacecraft charge; such a change would give us a new insight of the response time of the surrounding plasma and a deeper understanding on the plasma density based on the LP.

6. SUMMARY

In this paper, we have estimated the optical depth of Saturn's main rings in EUV wavelengths by measuring the changes in current measured by the LP when Cassini went into shadow behind the main rings. We found that the current reached noise level due to a reduction of the photoemission current in an amount proportional to the optical depth. During the eclipses by Saturn it was drawn very close to zero, almost down to noise level, but was variable during the eclipse by the rings, following the ring's transparency. Combining that change with the photoelectron yield of the LP coating material from the solar spectrum, we calculated the optical depth in the EUV, as the yield is more sensitive near Lyman-α. Our results are similar to previous studies that were done with Cassini's UVIS: The C and D rings are the most transparent (optically thin), while the B and A are the opaquest (optically thick).

The optical depth values we calculated compared with previous studies are: For the D ring, it is very close to 0 (agreeing with previous studies), for the C ring it is ~ 0.1 (agreeing with previous studies), for the B1 region it is ~ 2 (previous studies calculated ~ 1), for the B2 region it is ~ 2 (agreeing with previous studies), for B3 it is ~ 1.5 (agreeing with previous studies), for the Cassini Division it is ~ 0.1 (agreeing with previous studies), and for the A ring it is ~ 1 (previous studies calculated ~ 0.5). For the regions B4 and B5 of the B ring, we calculated $1-2$ (previous studies calculated ≥ 2) and ~ 1.75 (previous studies calculated $2-3$) respectively, but these results need to be used cautiously due to the limited sample size for these regions. The factors limiting our resolution was the sampling rate of the instrument and the low angle of the Sun with respect to the rings plane.

We estimate that the major reasons for the discrepancies are the limited available data, the rings material and structure, and the secondary electrons produced by the magnetospheric energetic electrons. The significance of this study is both the study of

the photoelectrons effect on the instrument but also the calculation of the main rings' optical depth using a plasma instrument. For future work, we will mainly focus on including data from more plasma instruments (e.g. CAPS), studying the high-energy electrons impact, and studying any diffraction and/or reflection effects.

These results are novel as we are able to use the LP—an instrument designed to measure the *in situ* properties of a plasma—to estimate the optical depth of Saturn's rings. This demonstrates an interdisciplinary use for the LP and is complementary to Brace et al. (1988) who showed that an LP instrument can provide estimates of time variation in solar EUV. Therefore, these ideas might be exploited for future mission design and operations that could take advantage of this opportunity through instrument placement on the spacecraft (to ensure that instrument shadowing was carried to calibrate the response of a LP to sunlight) and changing operating modes (e.g. adjusting sweep voltages and cadence during ring eclipses or occultations).

DATA AVAILABILITY

The LP data used in this work are available at the 'Planetary Data System: Planetary Plasma Interactions' (https://pds-ppi.igpp.ucla.edu/mission/Cassini-Huygens/CO/RPWS) (Wahlund, Kurth & Granroth, 2014). The times for the eclipses are presented in Appendix A.

REFERENCES

Acton C. H., 1996, Planet. Space Sci., 44, 65
Brace L. H., Hoegy W. R., Theis R. F., 1988, J. Geophys. Res., 93, 7282
Bradley T. J. et al., 2020, J. Geophys. Res.: Space Phys., 125, e27907
Coates A. J. et al., 2005, Geophys. Res. Lett., 32, L14S09
Colombo G., Goldreich P., Harris A., 1976, Nature, 264, 344
Colwell J. E., Brooks M., Jerousek R. G., Coleman C., Tiscareno M. S., Aye K.-M., Lewis M., Esposito L. W., 2021, AGU Fall Meeting 2021
Colwell J. E., Esposito L. W., Jerousek R. G., Sremčević M., Pettis D., Bradley E. T., 2010, Astron. J., 140, 1569
Colwell J. E., Esposito L. W., Sremčević M., 2006, Geophys. Res. Lett., 33, L07201
Colwell J. E., Esposito L. W., Sremčević M., Stewart G. R., McClintock W. E., 2007, Icarus, 190, 127
Colwell J. E., Nicholson P. D., Tiscareno M. S., Murray C. D., French R. G., Marouf E. A., 2009, in Dougherty M.K., Esposito L.W., Krimigis S.M., eds, Saturn from Cassini-Huygens, The Structure of Saturn's Rings. Springer, Dordrecht, p. 375
Diaz-Aguado M. F., Bonnell J. W., Bale S. D., Rezvani S. J., Koshmak K., Giglia A., Nannarone S., Gruntman M., 2018, J. Spacecr. Rockets, 56, 1
Dunn D. E., Molnar L. A., Niehof J. T., de Pater I., Lissauer J. J., 2004, Icarus, 171, 183
Esposito L. W. et al., 1983, J. Geophys. Res., 88, 8643

Esposito L. W. et al., 2004, Space Sci. Rev., 115, 299

Fahleson U., 1967, Space Sci. Rev., 7, 238

Farrell W. M., Kurth W. S., Gurnett D. A., Persoon A. M., MacDowall R. J., 2017, Icarus, 292, 48

Ferrari C., Brooks S., Edgington S., Leyrat C., Pilorz S., Spilker L., 2009, Icarus, 199, 145

Garnier P. et al., 2013, J. Geophys. Res.: Space Phys., 118, 7054

Grard R. J. L., 1973, J. Geophys. Res., 78, 2885

Gurnett D. A. et al., 2004, Space Sci. Rev., 114, 395

Gurnett D. A., Persoon A. M., Kurth W. S., Groene J. B., Averkamp T. F., Dougherty M. K., Southwood D. J., 2007, Science, 316, 442

Gustafsson G., Wahlund J.-E., 2010, Planet. Space Sci., 58, 1018

Hadid L. Z. et al., 2018, Geophys. Res. Lett., 45, 10084

Hadid L. Z. et al., 2019, Geophys. Res. Lett., 46, 9362

Hedman M. M., Nicholson P. D., Cuzzi J. N., Clark R. N., Filacchione G., Capaccioni F., Ciarniello M., 2013, Icarus, 223, 105

Hedman M. M., Nicholson P. D., Salo H., Wallis B. D., Buratti B. J., Baines K. H., Brown R. H., Cark R. N., 2007, AJ, 133, 2624

Henry R. C., 2002, ApJ, 570, 697

Hoegy W. R., Brace L. H., 1999, Rev. Sci. Instrum., 70, 3015

Holmberg M. K. G., Wahlund J.-E., Morooka M. W., Persoon A. M., 2012, Planet. Space Sci., 73, 151

Huebner W. F., Keady J. J., Lyon S. P., 1992, Astrophys. Space Sci., 195, 1

Ida S., 2019, Science, 364, 1028

Jacobsen K. S., Wahlund J.-E., Pedersen A., 2009, Planet. Space Sci., 57(1), 48

Jerousek R. G., Colwell J. E., Esposito L. W., Nicholson P. D., Hedman M. M., 2016, Icarus, 279, 36

Johnson R. E. et al., 2006, Icarus, 180, 393

Laframboise J. G., 1966, PhD thesis, Univ. Toronto

Matson D. L., Spilker L. J., Lebreton J.-P., 2002, Space Sci. Rev., 104, 1

McCluney W. R., 2014, Introduction to Radiometry and Photometry (Second ed), Artech House Applied Photonics Series. Artech House Publ., Boston, London

Mott-Smith H. M., Langmuir I., 1926, Phys. Rev., 28(4), 727

Nicholson P. D., French R. G., Campbell D. B., Margot J.-L., Nolan M. C., Black G. J., Salo H. J., 2005, Icarus, 177, 32

Nicholson P. D., Hedman M. M., 2010, Icarus, 206, 410

Persoon A. M. et al., 2019, Geophys. Res. Lett., 46, 3061

Persoon A. M. et al., 2020, J. Geophys. Res.: Space Phys., 125, e27545

Persoon A. M., Gurnett D. A., Kurth W. S., Groene J. B., 2006, Geophys. Res. Lett., 33(18), L18106

Pontius D. H., Hill T. W., 2006, J. Geophys. Res.: Space Phys., 111, A09214

Provan G., Cowley S. W. H., Bunce E. J., Milan S. E., Persoon A. M., Gurnett D. A., 2021, J. Geophys. Res.: Space Phys., 126, e29332

Salo H., Karjalainen R., French R. G., 2004, Icarus, 170, 70

Thomsen M. F., Coates A. J., Roussos E., Wilson R. J., Hansen K. C., Lewis G. R., 2016, J. Geophys. Res.: Space Phys., 121, 5436

Tseng W.-L., Johnson R. E., Thomsen M. F., Cassidy T. A., Elrod M. K., 2011, J. Geophys. Res.: Space Phys., 116, 2011

Wahlund J.-E, Kurth W. S., Granroth L.J., 2014, CASSINI RPWS LANG-MUIR PROBE POTENTIAL CURRENT DATA, NASA Planetary Data System

Wahlund J.-E. et al., 2018, Science, 359, 66

Whalström M. K., Johansson E., Veszelei E., Bennich P., Olsson M., Hogmark S., 1992, Thin Solid Films, 220, 315

Whipple E. C., 1981, Rep. Prog. Phys., 44, 1197

William D. R., 1995, 17 July, Saturnian Rings Fact Sheet. https://nssdc.gsfc.nasa.gov/planetary/factsheet/satringfact.html(accessed Jan 23)

Withers P., Jakosky B. M., 2016, J. Geophys. Res.: Space Phys., 122, 802

APPENDIX A: THE DATA OF THE ECLIPSES BY SATURN AND THE RINGS

Here, follow tables with all the data of the eclipses by Saturn and the rings we found. Table A1 shows the solar eclipses of Saturn, Table A2 shows the periods overlapping eclipses by the rings and Saturn, and Table A3 shows the eclipses by rings that did not overlap with an eclipse by Saturn; for better understanding on the overlapping eclipses a schematic of the interaction between the eclipses by Saturn and by the rings is presented in Fig. 5. We must mention that for rev. 271–286 there were two eclipses by the rings: one close to the periapsis and one close to the apoapsis; they are marked as 'a' and 'b', e.g. 271a and 271b.

Table A1. Eclipses by Saturn. The first column shows the number of the eclipse. The second column shows the rev. number in which the eclipse took place. The third column shows the time the eclipse started, in UT (rounded to the closest minute). The fourth column shows the duration of the eclipse in minutes. The fifth column shows the data resolution type: 'L' is for low-resolution data, i.e. when the LP was conducting one sweep every ~10 min, 'H' is for high-resolution data, i.e. the LP was conducting one sweep every ~30 s, and 'mixed' is when the LP rate changed during the eclipse and there are both high- and low-resolution data, and 'no data' is the eclipses without data. The sixth column denotes whether there was an interaction with an eclipse by the rings during the eclipse by Saturn, i.e. when Cassini was already in the rings' shadow while it was entering in Saturn's shadow. The asterisk for rev. 70–75 denotes that these eclipses by the rings were done completely in Saturn's shadow. A schematic of the interaction between the Saturn and the rings eclipses can be seen in Fig. 5.

#	Rev	Beginning time	Duration (min)	Low/High resolution	Interaction with eclipse by rings?
1	7	2005–05-03 05:10	152	L	—
2	8	2005–05-21 09:33	153	L	—
3	9	2005–06-08 14:10	154	L	—
4	10	2005–06-26 19:20	155	L	—
5	11	2005–07-15 01:52	156	L	—
6	12	2005–08-02 09:32	157	L	—
7	13	2005–08-20 15:01	157	L	—
8	14	2005–09-05 14:37	136	L	Y
9	28	2006–09-15 08:45	866	No data	Y
10	44	2007–05-10 15:22	134	L	Y
11	45	2007–05-26 19:39	137	H	Y
12	46	2007–06-11 21:07	119	H	—
13	47	2007–06-27 22:10	90	L	—
14	50	2007–09-30 07:16	54	H	—
15	51	2007–10-24 05:05	72	H	—
16	52	2007–11-17 05:02	76	L	—
17	53	2007–12-03 06:10	83	L	Y
18	54	2007–12-19 03:06	75	Mixed	Y
19	56	2008–01-15 20:33	59	L	Y
20	57	2008–01-27 18:47	56	Mixed	Y
21	58	2008–02-08 17:23	59	H	Y
22	59	2008–02-20 17:25	56	H	Y
23	68	2008–05-17 22:44	29	L	—
24	69	2008–05-25 21:59	22	L	Y
25	70	2008–06-01 21:53	53	L	Y*
26	71	2008–06-09 01:12	51	Mixed	Y*
27	72	2008–06-16 04:20	50	Mixed	Y*
28	73	2008–06-23 07:26	48	L	Y*
29	74	2008–06-30 08:17	46	L	Y*
30	75	2008–07-07 09:07	44	L	Y*
31	76	2008–07-14 09:58	42	L	—
32	77	2008–07-21 10:53	39	L	Y
33	78	2008–07-28 11:53	36	L	Y
34	119	2009-10-13 14:58	275	No data	—
35	120	2009–11-01 14:35	270	L	—
36	121	2009–11-20 15:19	266	L	—
37	122	2009–12-09 16:19	261	L	—
38	123	2009–12-25 20:42	210	H	—
39	125	2010–01-26 19:15	212	L	—
40	126	2010–02-13 05:58	221	L	—
41	127	2010–03-02 19:12	216	H	—
42	128	2010–03-20 10:34	211	No data	—
43	129	2010–04-07 00:56	199	No data	—
44	130	2010–04-27 09:49	197	L	—
45	131	2010–05-17 20:57	182	No data	—
46	133	2010–06-19 00:16	173	H	—
47	135	2010–07-24 15:59	224	No data	Y
48	136	2010–08-13 13:55	221	Mixed	Y
49	137	2010–09-02 14:36	217	No data	Y
50	138	2010–09-22 13:04	213	L	—
51	139	2010–10-16 03:21	190	No data	—
52	140	2010-11-09 04:00	173	No data	—
53	141	2010–11-29 23:59	66	L	—
54	142	2010–12-20 13:39	30	L	—
55	150	2011–07-10 12:12	56	H	—

Table A1 – *continued*

#	Rev	Beginning time	Duration (min)	Low/High resolution	Interaction with eclipse by rings?
56	151	2011–08-01 04:31	47	L	—
57	152	2011–08-23 00:23	38	L	—
58	153	2011–09-13 19:42	73	L	—
59	154	2011–10-01 13:35	70	H	—
60	155	2011–10-19 09:08	67	H	—
61	156	2011–11-06 04:45	63	H	—
62	157	2011–11-24 01:22	60	H	—
63	158	2011–12-11 22:55	58	L	—
64	167	2012–06-05 00:29	115	L	Y
65	168	2012–06-28 13:08	143	No data	Y
66	169	2012–07-22 11:56	125	No data	Y
67	170	2012–08-12 11:01	211	No data	Y
68	171	2012–09-02 17:18	207	No data	Y
69	172	2012–09-24 00:48	201	No data	Y
70	173	2012–10-17 05:15	274	No data	Y
71	174	2012–11-10 03:52	274	No data	Y
72	175	2012–11-26 08:57	198	No data	Y
73	176	2012–12-09 09:30	116	No data	—
74	177	2012–12-22 15:38	139	No data	—
75	178	2013–01-04 22:09	156	No data	Y
76	179	2013–01-18 05:09	171	No data	Y
77	180	2013–01-31 12:22	182	No data	Y
78	181	2013–02-13 19:39	191	No data	Y
79	182	2013–02-25 11:06	159	No data	Y
80	183	2013–03-09 10:11	171	No data	Y
81	184	2013–03-21 09:11	182	No data	Y
82	185	2013–04-02 08:11	190	No data	Y
83	186	2013–04-12 03:48	147	No data	Y
84	187	2013–04-21 17:28	151	No data	Y
85	188	2013–05-01 07:09	154	No data	Y
86	189	2013–05-10 20:47	157	No data	Y
87	190	2013–05-20 10:32	160	L	Y
88	191	2013–05-31 06:01	231	No data	Y
89	192	2013–06-12 04:57	236	No data	Y
90	193	2013–06-24 04:07	239	No data	—
91	194	2013–07-06 03:10	239	No data	—
92	195	2013–07-19 22:12	284	No data	Y
93	237	2016–06-30 03:25	253	No data	Y
94	238	2016–07-24 02:19	246	No data	Y
95	239	2016–08-08 22:46	225	No data	Y
96	242	2016–09-13 18:52	29	No data	Y
97	243	2016–09-25 17:22	114	No data	Y
98	256	2017–01-10 02:18	46	No data	Y
99	257	2017–01-17 05:35	136	No data	Y
100	258	2017–01-24 09:14	182	No data	Y
101	259	2017–01-31 13:02	221	No data	Y
102	260	2017–02-07 17:22	255	No data	Y
103	261	2017–02-14 21:50	281	No data	Y
104	262	2017–02-22 01:38	305	No data	Y
105	263	2017–03-01 05:44	324	No data	Y
106	264	2017–03-08 09:39	339	No data	Y
107	265	2017–03-15 13:35	353	No data	Y
108	266	2017–03-22 17:29	365	No data	Y
109	267	2017–03-29 21:22	374	No data	Y
110	268	2017–04-06 01:18	383	No data	Y
111	269	2017–04-13 05:23	389	No data	Y
112	270	2017–04-20 09:33	394	No data	Y
113	271b	2017–04-26 14:33	399	No data	Y
114	272b	2017–05-03 01:24	391	No data	Y
115	273b	2017–05-09 12:12	375	No data	Y
116	274b	2017–05-15 23:00	347	No data	Y
117	275b	2017–05-22 09:56	300	No data	Y
118	276b	2017–05-28 22:02	207	No data	Y

Table A2. Interacting eclipses by both Saturn and the rings. The first column shows the number of the eclipse. The second column shows the rev. number in which the eclipse took place. The third column shows the eclipse data type. 'L' is for low-resolution data, i.e. when the LP was conducting one sweep every ~10 min, 'H' is for high-resolution data, i.e. the LP was conducting one sweep every ~30 s, 'inconcl.' is when the data are not well structured so it is inconclusive on what type of data they are, e.g. when there are gaps longer than 10 min in the data, 'no data' is when the LP had no data during the eclipse, and 'blocked' is when the eclipse by the rings took place in an ongoing eclipse by Saturn; this applies for rev. 70–75.

#	Rev	Low/high resolution
1	14	L
2	28	No data
3	44	L
4	45	H
5	53	Inconcl.
6	54	H
7	56	L
8	57	H
9	58	H
10	59	H
11	69	Inconcl.
12	70	Blocked
13	71	Blocked
14	72	Blocked
15	73	Blocked
16	74	Blocked
17	75	Blocked
18	77	No data
19	78	No data
20	135	L
21	136	H
22	137	No data
23	167	L
24	168	No data
25	169	No data
26	170	No data
27	171	No data
28	172	No data
29	173	No data
30	174	No data
31	175	No data
32	178	No data
33	179	No data
34	180	No data
35	181	No data
36	182	No data
37	183	No data
38	184	No data
39	185	No data
40	186	No data
41	187	No data
42	188	No data
43	189	No data
44	190	Inconcl.
45	191	No data
46	192	No data
47	195	No data
48	237	No data
49	238	No data
50	239	No data
51	242	No data
52	243	No data
53	256	No data
54	257	No data
55	258	No data

Table A2 *– continued*

#	Rev	Low/high resolution
56	259	No data
57	260	No data
58	261	No data
59	262	No data
60	263	No data
61	264	No data
62	265	No data
63	266	No data
64	267	No data
65	268	No data
66	269	No data
67	270	No data
68	271b	No data
69	272b	No data
70	273b	No data
71	274b	No data
72	275b	No data
73	276b	No data

Table A3. Eclipses by the rings without an overlapping eclipse by Saturn. The columns are the same as in Table A2.

#	Rev	Low/high resolution
1	6	L
2	7	L
3	8	L
4	9	L
5	10	L
6	11	L
7	12	L
8	13	L
9	43	No data
10	46	H
11	55	Mixed
12	60	H
13	61	No data
14	62	H
15	63	H
16	64	H
17	65	H
18	66	H
19	67	H
20	68	L
21	76	No data
22	79	L
23	80	H
24	81	L
25	82	Mixed
26	83	L
27	84	L
28	85	L
29	86	L
30	87	H
31	88	H
32	89	Inconcl.
33	90	L
34	91	Mixed
35	92	L
36	93	L
37	94	L
38	95	Inconcl.
39	176	No data

Table A3 – *continued*

#	Rev	Low/high resolution
40	177	No data
41	236	No data
42	240	No data
43	241	No data
44	244	No data
45	245	No data
46	246	No data
47	247	No data
48	248	No data
49	249	No data
50	250	No data
51	251	No data
52	252	No data
53	253	No data
54	254	No data
55	255	No data
56	271a	H
57	272a	H
58	273a	H
59	274a	Mixed
60	275a	Mixed
61	276a	Mixed
62	277a	H
63	277b	No data
64	278a	H
65	278b	No data
66	279a	H
67	279b	No data
68	280a	Inconcl.
69	280b	No data
70	281a	No data
71	281b	No data
72	282a	H
73	282b	No data
74	283a	H
75	283b	No data
76	284a	H
77	284b	No data
78	285a	No data
79	285b	No data
80	286a	No data
81	286b	No data
82	287	H
83	288	Inconcl.
84	289	H
85	290	H
86	291	Inconcl.
87	292	H

APPENDIX B: DEFINITION OF THE MAIN RINGS OPTICAL DEPTH WITH LP CURRENT DATA

The LP photoemission current can be given as

$$I_{ph} = A_{LP} j_{ph} = \pi r_{LP}^2 j_{ph} \tag{B1}$$

where j_{ph} is the photoemission current density, and $A_{LP} = \pi r_{LP}^2$ is the probe area. The photoemission current density is

$$j_{ph} = e \int_0^\infty Y(\lambda) H(\lambda) \, d\lambda \tag{B2}$$

where e is the electron charge, $Y(\lambda)$ is the yield of photoelectrons (units of photoelectrons per photon), and $H(\lambda)$ is the flux of photons per unit wavelength (units of photons per square metre per seconds per metre/wavelength).

The spectral flux density $E_{e,\lambda}$ is the energy flux per unit wavelength (units of Watt per square metre per metre; $\mathrm{W\,m^{-2}\,m^{-1}}$) and it is related to $H(\lambda)$ by the energy of a photon at a particular wavelength, hc/λ:

$$H(\lambda) = E_{e,\lambda} \frac{\lambda}{hc} \tag{B3}$$

hence:

$$I_{ph} = \frac{e}{hc} \int_0^\infty Y(\lambda) A_p E_{e,\lambda} \lambda \, d\lambda. \tag{B4}$$

Fig. B1 shows the photoemission spectrum from the LP—effectively the integrand of (B4). The first panel is the yield of the annealed titanium nitride (Diaz-Aguado et al. 2018), which is the LP coating, the second panel is the solar spectrum (Huebner, Keady & Lyon 1992), and the third shows the photoemission spectrum for the LP, i.e. the multiplication of the first panel with the second. The total photoemission is about 32.5×10^9 photoelectrons per square centimetre per second. The long wavelengths carry about 20 per cent of that number, while the short wavelengths have about 2 per cent of the photoelectrons. The Lyman-a line emits around 60 per cent of the total photoelectrons, while the rest of the Lyman series emit around 10 per cent, and the Lyman continuum around 6 per cent.

We must note that besides the solar radiation there is an additional source radiation that could affect the LP photoemission: the local interstellar radiation. Focusing in the region around the Lyman-a emission, at ~ 121.6 nm—as the photoemission contribution is considerably higher than the rest of the wavelengths—we calculated the solar radiation to be $\sim 2 \times 10^{10}$ photons $\mathrm{cm^{-2}\,s^{-1}\,bin^{-1}}$ (third

panel of Fig. B1). The bin width for this wavelength is about 0.75 nm($= 7.5$ Å), so the solar radiation flux is $\sim 2.7 \times 10^9$ photons $\mathrm{cm^{-2}\,s^{-1}\,\mathring{A}^{-1}}$. Henry (2002) showed that the maximum flux for this wavelength in the—unrealistic—case where no radiation is lost due to any processes (all the scattered radiation remains part of the interstellar radiation field and the interstellar grain is fully reflective) is around 1.3×10^6 photons $\mathrm{cm^{-2}\,s^{-1}\,\mathring{A}^{-1}}$. This is at least three orders of magnitude smaller than the solar flux spectrum, hence its contribution can be neglected.

Equation (B4) mirrors similar expressions in optical remote sensing where the measured pixel intensity is an integration of an instrument response function over a signal as a function of wavelength. We define $R(\lambda) = Y(\lambda)\lambda$ as a response function for how much current is produced, per unit wavelength, due to a spectral radiant flux $\Phi_{e,\lambda}$. We note that the High-Speed Photometer (HSP) in the UVIS—often used for UV opacity and structure studies of Saturn's rings (e.g. Colwell et al. 2007, 2010)—has a short-wavelength cutoff of 110 nm (e.g. Esposito et al. 2004; Colwell et al. 2007), so our response function slightly overlaps that of HSP but crucially we extend much further into the EUV. If we take the ratio of the photoemission current out of eclipse (incident), I_{ph}^i, to that in an eclipse (transmitted), I_{pe}^t, we get

$$\frac{I_{pe}^i}{I_{pe}^t} = \frac{\int_0^\infty R(\lambda) \Phi_{e,\lambda}^i \, d\lambda}{\int_0^\infty R(\lambda) \Phi_{e,\lambda}^t \, d\lambda}. \tag{B5}$$

The optical depth is defined as the ratio of the incident radiant flux, Φ_e^i, to the transmitted radiant flux Φ_e^t

$$\tau = \ln \frac{\Phi_e^i}{\Phi_e^t} \tag{B6}$$

where the radiant flux is a wavelength integral of the spectral radiant flux, $\Phi_{e,\lambda}$ (units of Watt per metre)

$$\Phi_e = \int_0^\infty \Phi_{e,\lambda} \, d\lambda. \tag{B7}$$

Therefore, from equations (B5), (B6), and (B7), the ratio of the current is equal to the (weighted by instrument response) ratio of the radiant flux, which mirrors the methodology used in other studies that determined the optical depth (e.g. Colwell et al. 2010):

$$\tau = \ln \frac{\Phi_e^i}{\Phi_e^t} = \ln \frac{I_{pe}^i}{I_{pe}^t}. \tag{B8}$$

This paper has been typeset from a T$_{\mathrm{E}}$X/L$^{\mathrm{A}}$T$_{\mathrm{E}}$X file prepared by the author.
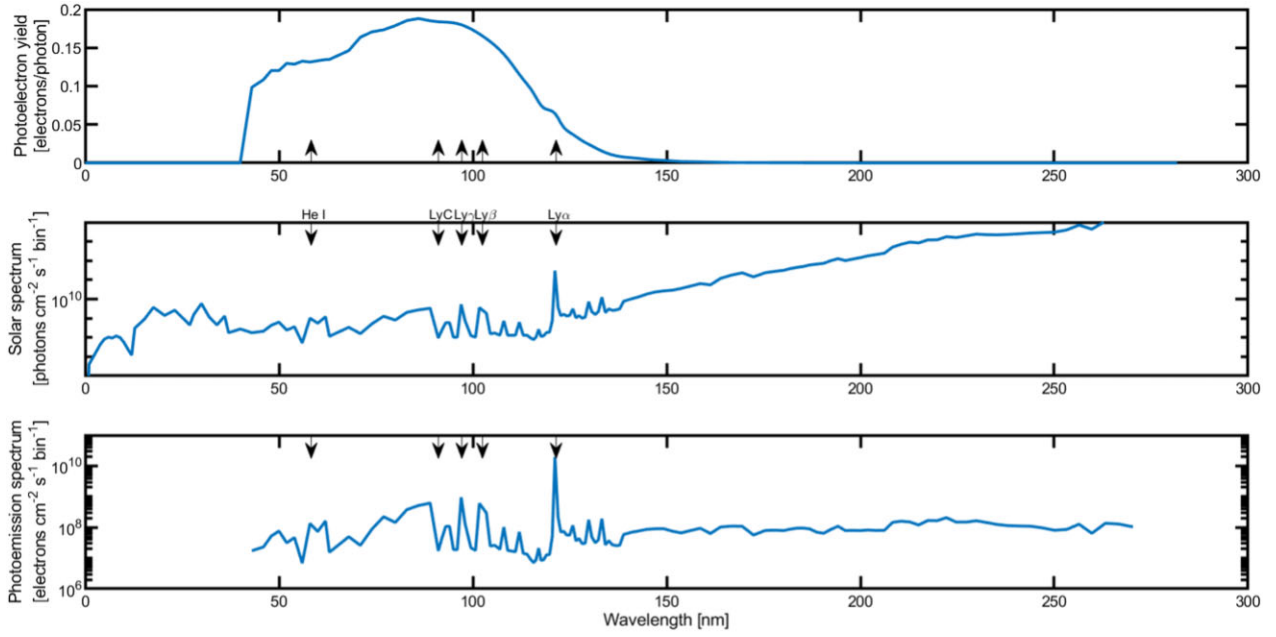
Figure B1. The photoemission spectrum of the Cassini LP at Saturn. Top panel: The photoelectron yield of titanium nitride matching the coating for the LP. Middle panel: The solar spectrum. Bottom panel: A multiplication of the two gives the photoemission spectrum for the LP. The majority of the photoelectrons are generated in Lyman-a.